



저작자표시-비영리-변경금지 2.0 대한민국

이용자는 아래의 조건을 따르는 경우에 한하여 자유롭게

- 이 저작물을 복제, 배포, 전송, 전시, 공연 및 방송할 수 있습니다.

다음과 같은 조건을 따라야 합니다:



저작자표시. 귀하는 원저작자를 표시하여야 합니다.



비영리. 귀하는 이 저작물을 영리 목적으로 이용할 수 없습니다.



변경금지. 귀하는 이 저작물을 개작, 변형 또는 가공할 수 없습니다.

- 귀하는, 이 저작물의 재이용이나 배포의 경우, 이 저작물에 적용된 이용허락조건을 명확하게 나타내어야 합니다.
- 저작권자로부터 별도의 허가를 받으면 이러한 조건들은 적용되지 않습니다.

저작권법에 따른 이용자의 권리는 위의 내용에 의하여 영향을 받지 않습니다.

이것은 [이용허락규약\(Legal Code\)](#)을 이해하기 쉽게 요약한 것입니다.

[Disclaimer](#)

공학박사 학위논문

**Studies on Highly Active and Durable Pt Nanocluster
and PdFe Nanoparticles for Polymer Electrolyte Membrane
Fuel Cells**

고분자 전해질 연료전지용 고효성 고안정성 백금 나노클러스터와
팔라듐철 나노입자 연구

2013년 8월

서울대학교 대학원

공과대학 화학생물공학부

최 광 현

**Studies on Highly Active and Durable Pt Nanocluster
and PdFe Nanoparticles for Polymer Electrolyte Membrane
Fuel Cells**

고분자 전해질 연료전지용 고효성 고안정성 백금 나노클러스터와
팔라듐철 나노입자 연구

지도교수 성 영 은

이 논문을 공학박사학위논문으로 제출함

2013년 8월

서울대학교 대학원
공과대학 화학생물공학부
최 광 현

최광현의 박사학위논문을 인준함

2013년 8월

위 원 장	<u>이 종 협</u>	(인)
부 위 원 장	<u>성 영 은</u>	(인)
위 원	<u>김 도 희</u>	(인)
위 원	<u>탁 용 석</u>	(인)
위 원	<u>유 성 중</u>	(인)

Abstract

Proton exchange membrane fuel cell (PEMFC) is an electrochemical energy conversion device that uses hydrogen and oxygen as fuel. PEMFC can convert chemical energy directly to electricity without any mechanical process. Because of this advantage it is much more efficient than combustion engine. However, there are several disadvantages of PEMFC that preclude any further commercialization. Those problems are related to fuel reforming and storage, operation conditions, membrane electrode assembly, and device fabricating procedure, but the heaviest problems are high stability and high activity of the catalyst. Especially for PEMFC there is a large overpotential loss phenomenon in the cathode. Due to this overpotential, in a low current density region charge transfer resistance for the sluggish oxygen reduction reaction has been detected. To avert this problem many researchers have focused on synthesizing PtM (M = Fe, Co, Ni) alloyed, core-shell structured, and various shape controlled nanocatalysts.

It is considered that nanocatalysts with particular facets, such as (111) and (110) can shed a new light on obtaining high stability and high activity for the PEMFC. To enhance the stability and ORR activity of Pt itself, Pt cluster, a 20-30 nm nanostructure that is formed by 5 nm nanoparticles, was synthesized. The Pt cluster was oriented by using a capping agent containing amine ligand and heat control. The characterization of morphology, crystalline structure, and surface structures were mainly studied by

transmission electron microscopy (TEM), X-ray diffraction (XRD), X-ray photoelectron spectroscopy (XPS), and CO oxidation current measurement. In addition, the effect of high coordination and lattice contraction on Pt cluster structure was confirmed by the X-ray absorption near-edge structure (XANES) and extended X-ray absorption fine structure (EXAFS). The formation of (111) facets, high coordination structure, and lattice contraction induced high stability and high activity towards ORR. Secondly, to cut down the cost of the Pt catalyst Pt alloyed with cheap transition metals such as Ni, Fe, Co have been studied. Among those alloy nanoparticles PtNi is one of the best well know catalyst that has higher ORR activity than Pt. However, PtNi itself suffers from low stability which originates from fast dissolution of Ni. In this thesis we report a urchin like PtNi nanostructure that has a high stability and high ORR activity in comparison with commercial PtNi. The characterization of morphology, crystalline structure, and surface structures were mainly studied by TEM, XRD, XPS, and CO oxidation current measurement.

In third, to avoid using substantial amount of Pt many researchers did empirical and theoretical studies of scrutinizing PdM (M = Fe, Co, Ni, Cu) alloyed and PdM core-Pt shell (PdM@Pt) nanocatalysts. Theoretical calculation results by former researchers announce Pd-skin PdFe-core can have a similar ORR activity with Pt and PdFe@Pt possesses high potential for strong stability. Therefore, we applied this theoretical result and synthesized the proper PdFe core and decorating Pt on the surface of the core by hydroquinone method. To make Pd-skin PdFe-core structure from the pristine PdFe

nanoparticles post heat treatment was chosen. The heat procedure started with removing the carbon by heating the pristine PdFe up to 200 °C in air flow for 1h 30 min. After the reaction the sample was heated up to 500 °C in H₂ flow for 2 h. The morphology, crystalline structure, and surface structures of Pd-skin PdFe-core sample were mainly analyzed by TEM, XRD, XPS, and CO oxidation current measurement. In addition, the ORR activity of Pd-skin PdFe-core exhibited remarkable enhancement in comparison with that of pristine PdFe.

PdFe was decorated with Pt to preserve the high activity even after a long term cycling. The surface property of the PdFe@Pt was verified by cyclic voltammetry (CV) and CO oxidation measurement. The retention of ORR activity of PdFe@Pt was confirmed by ADT test followed by 4,000 cycles.

These structure modifications of fuel cell catalysts could give enhancement of the electrochemical property, stability and catalytic activity in PEMFC. In addition, we need an empirical and theoretical harmony for understanding these enhancements and finding the most suitable catalyst that possess high stability and high activity for PEMFC.

Keywords: fuel cell, cluster, urchin like, core-shell, oxygen reduction reaction, stability

Student Number: 2009-31266

Contents

Abstract	i
List of Tables	vi
List of Tables	vii
Chapter 1. Introduction	1
1.1 Fuel cell basics.....	1
1.1.1 Categorization of Fuel Cells.....	1
1.1.2 Polymer electrolyte membrane fuel cell	4
1.2 Concepts of Study	9
1.3 References	11
Chapter 2. Experimental	14
2.1 Catalyst preparation	14
2.1.1 Synthesis of Pt cluster	14
2.1.2 Urchin like PtNi nanostructures	15
2.1.3 Synthesis of PdFe nanoparticles.....	16
2.1.4 Pd-rich PdFe alloyed nanoparticles by post treatment	17
2.1.5 PdFe-core nanoparticles@Pt-decoration.....	17
2.2 Physical and electronic structure measurements.....	18
2.2.1 X-ray diffraction.....	18
2.2.2 Transmission electron microscopy	19
2.2.3 X-ray absorption spectroscopy (XAS)	20
2.3 Electrochemical characterizations	24
2.3.1 Cyclic voltammetry and Rotating disk electrode	24
2.3.2 CO electrooxidation	28
2.4 References.....	31
Chapter 3. Results and discussion	32

3.1 Cluster Shaped Nanocatalysts	32
3.1.1 Pt nanocluster structure.....	32
3.1.2 Crystalline and surface structure of Pt cluster	34
3.1.3 Electrochemical characterization of Pt cluster	35
3.2 Urchin like PtNi nanostructure.....	47
3.2.1 Urchin like PtNi nanostructure	47
3.2.2 Crystalline and surface structure of urchin like PtNi	50
3.2.3 Electrochemical characterization of urchin like PtNi	51
3.3 Carbon supported PdFe nanoparticles	63
3.3.1. PdFe nanocatalyst	63
3.3.2 Crystalline structure of PdFe after heat treatment.....	64
3.3.3. Electrochemical characterization of PdFe after heat treatment.....	66
3.3.4 XANES characterization of PdFe after heat treatment.....	67
3.4 Pt decorated on PdFe core nanoparticles	78
3.4.1. Carbon supported PdFe@Pt nanoparticles.....	78
3.4.2. Crystalline and surface structure of Carbon supported PdFe@Pt nanoparticles ..	79
3.4.3. Electrochemical characterization of Carbon supported PdFe@Pt nanoparticles..	79
3.5 References.....	87
Chapter 4. Conclusions	92
국 문 초 록	97

List of Tables

Table 3.1	Lattice parameter values for PdFe samples.....	71
Table 3.2	_FWHM and particle size values for Pt decorated PdFe 3:1 300 °C H ₂ 3hr	84

List of Figures

Fig. 1.1	Applications of fuel cells.....	3
Fig. 1.2	Scheme of PEMFC operation.....	6
Fig. 1.3	Overall reaction of anode and cathode reaction in PEMFC.....	7
Fig. 1.4	Polarization curve of anode and cathode reaction in PEMFC.....	8
Fig. 2.1	Beamline map in the PAL. From the webpage, http://pal.postech.ac.kr	22
Fig. 2.2	Three main regions of X-ray absorption spectroscopy.....	23
Fig. 2.3	Profile of cyclic voltammetry.....	26
Fig. 2.4	Scheme of rotating disk electrode.....	27
Fig. 2.5	Scheme of Langmuir-Hinshelwood mechanism.....	30
Fig. 3.1	TEM images of Pt cluster.....	39
Fig. 3.2	XRD of Pt cluster and commercial Pt.....	40
Fig. 3.3	TEM images of Pt cluster after 10,000 cycles ADT test.....	41
Fig. 3.4	Cyclic voltammetry of Pt cluster and Pt/C J.M.....	42
Fig. 3.5	ORR polarization curve of Pt cluster and Pt/C J.M.....	43
Fig. 3.6	CO _{chem} oxidative stripping voltammograms of Pt cluster and Pt/C J.M.....	44
Fig. 3.7	Cyclic voltammogram of Pt cluster and Pt/C J.M. after ADT test.....	45
Fig. 3.8	ORR polarization curve of Pt cluster and Pt/C J.M. after ADT.....	46
Fig. 3.9	TEM and EDX of urchin like Pt ₃ Ni nanostructure.....	54
Fig. 3.10	Scheme of synthesis of urchin like Pt _x Ni with one dimension.....	55
Fig. 3.11	X-ray diffraction pattern of Pt ₃ Ni, Pt ₂ Ni, and Pt ₁ Ni.....	56
Fig. 3.12	X-ray diffraction pattern of Pt ₃ Ni and Pt ₃ Ni E-tek.....	57
Fig. 3.13	Oxygen polarization curves of Pt _x Ni and cyclic voltammetry of urchin like Pt ₃ Ni and Pt ₃ Ni E-tek.....	58
Fig. 3.14	Specific and mass activity of Pt ₃ Ni and Pt ₃ Ni E-tek.....	59
Fig. 3.15	Cyclic voltammetry of Pt ₃ Ni and Pt ₃ Ni E-tek after 4000 cycles ADT test.....	60
Fig. 3.16	Oxygen polarization curves of Pt ₃ Ni and Pt ₃ Ni E-tek after 4000 cycles ADT test.....	61
Fig. 3.17	XANES spectra of (a) Pt L _{III} edge and (b) Ni K edge for urchin like Pt ₃ Ni	

and Pt ₃ Ni E-tek ₂	62
Fig. 3.18 XRD profiles of pristine PdFe samples.....	69
Fig. 3.19 Scheme of obtaining Pd rich surface by heat treatment.	70
Fig. 3.20 TEM images of pristine, 300 °C, and 500 °C post heat treated PdFe samples (a)(b)(c) Pd ₃ Fe ₁ , (d)(e)(f) Pd ₁ Fe ₁ , (g)(h)(i) Pd ₁ Fe ₃	72
Fig. 3.21 XRD profiles of pristine, 300 °C, and 500 °C post heat treated PdFe samples ₂ .	73
Fig. 3.22 XANES spectra of Pd K edge pristine, 300 °C, and 500 °C post heat treated PdFe samples.....	74
Fig. 3.23 XANES spectra of Fe K edge pristine, 300 °C, and 500 °C post heat treated PdFe samples.....	75
Fig. 3.24 Cyclic voltammetry of pristine PdFe and 500 °C post heat treated PdFe samples.	76
Fig. 3.25 Oxygen polarization curves and mass activity of pristine, 300 °C, and 500 °C post heat treated PdFe samples.	77
Fig. 3.26 Computational screening of Pt coated suitable core materials for the high activity and durability [64].	82
Fig. 3.27 XRD profiles of Pt decorated PdFe 3:1 300 °C H ₂ 3hr.	83
Fig. 3.28 Cyclic voltammograms and ORR polarization curves of Pt decorated PdFe 3:1 300 °C H ₂ 3hr ₂	85
Fig. 3.29 CO and CO ₂ oxidation curves of Pt decorated PdFe 3:1 300 °C H ₂ 3hr.....	86

Chapter 1

Introduction

1.1 Fuel cell basics

1.1.1. Categorization of Fuel Cells

A fuel cell is an electrochemical device that can convert the chemical energy of a reaction directly into electrical energy. A fuel cell is in some parts similar to a battery. It has an anode, cathode, and electrolyte, and it generates direct current electricity through electrochemical reactions. However, some aspects of a fuel cell are different to a battery; a fuel cell requires a constant feed of fuel and oxygen, and cannot be discharged as long as reactants are supplied. Fuel cells have the numerous advantages, such as low emission of pollutants, higher energy efficiency and reliability [1]. The reaction mechanism of fuel cell system is between hydrogen and oxygen. Various types of fuel cells have been studied by many researchers, as a new energy source, because they have many advantages [2]. Nevertheless, there is still cumbersome phenomenon for fuel cell to prevail in industry. These fuel cells can be categorized into five types according to their electrolytes; alkaline fuel cells (AFC), phosphoric acid fuel cells (PAFC), solid oxide fuel cells, molten carbonate fuel cells (MCFC), and polymer electrolyte membrane fuel cells (PEMFC). The

indispensable characteristic of the PEMFC is the simplicity. The electrolyte is a solid polymer (Nafion), which is intrinsically immobile. These fuel cells operate at relatively low temperatures. Due to this feature not like the other fuel cells PEMFC can be applied to both electric vehicles and portable devices such as cell phones, digital cameras, and laptop computers (Fig. 1.1).

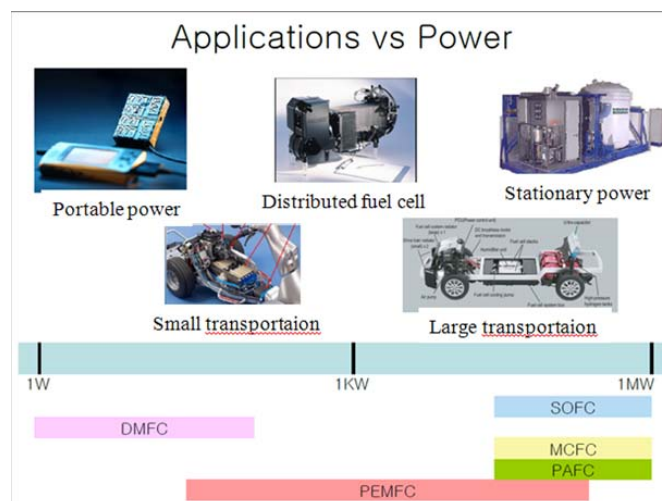


Fig. 1.1 Applications of fuel cells

1.1.2 Polymer electrolyte membrane fuel cell

As mentioned above PEMFC can be applied to both electric vehicles and portable devices such as cell phones, digital cameras, and laptop computers due to high coverage of various working voltages and various electric powers. The operation of PEMFC is initiated by injecting H₂ in anode and O₂ in cathode as a fuel (Fig. 1.2). In anode involved electrochemical reaction is the hydrogen oxidation reaction (HOR) which produces 2 protons and 2 electrons from a hydrogen molecule. HOR is a very rapid reaction which is a counterpart reaction of hydrogen evolution reaction. By and large, HOR mechanism is explained from three elementary reactions: Tafel reaction (dissociative adsorption of hydrogen molecule without electron transfer), Heyrovsky reaction (dissociative adsorption of hydrogen molecule with electron transfer), and Volmer reaction (desorption of hydrogen atom with charge transfer). However, improvement of HOR still does not provide enough power to overcome the power loss of PEMFC due to high overpotential in cathode. In cathode, the electrochemical reduction reaction involves oxygen molecule which produces water. The oxygen reduction reaction (ORR) is highly irreversible reaction in acidic condition, unlike HOR, with low exchange current density (range of 10⁻¹⁰-10⁻¹¹ A cm_{Pt}⁻²).

The overall reaction of PEMFC (Fig. 1.3) is governed by the overpotential in anode, cathode, and electrolyte which follows the equation;

$$E = E_0 - \eta_{act,a} - \eta_{act,c} - \eta_{ohm} - \eta_{mt,a} - \eta_{mt,c} \quad (1-1)$$

E_0 is the thermodynamic reversible potential, and the other terms can be divided into two categories one is charge transfer related overpotential and the other is mass transfer related overpotential. For The terms $\eta_{act,a}$ and $\eta_{act,c}$ are the activation overpotentials related to the charge transfer in the anode and cathode, respectively. The terms η_{ohm} is the ohmic overpotential in the cell, $\eta_{mt,a}$ and $\eta_{mt,c}$ are the mass transfer overpotentials in the anode and cathode, respectively. Among above overpotentials it has been known that $\eta_{act,c}$, the slow ORR, is the main reasons for potential losses during the PEMFC operation. The polarization curve of PEMFC is shown in Fig. 1.4. In the figure large potential losses in the low and high potential area, which are induced due to the charge transfer resistance of the ORR is well depicted [2].

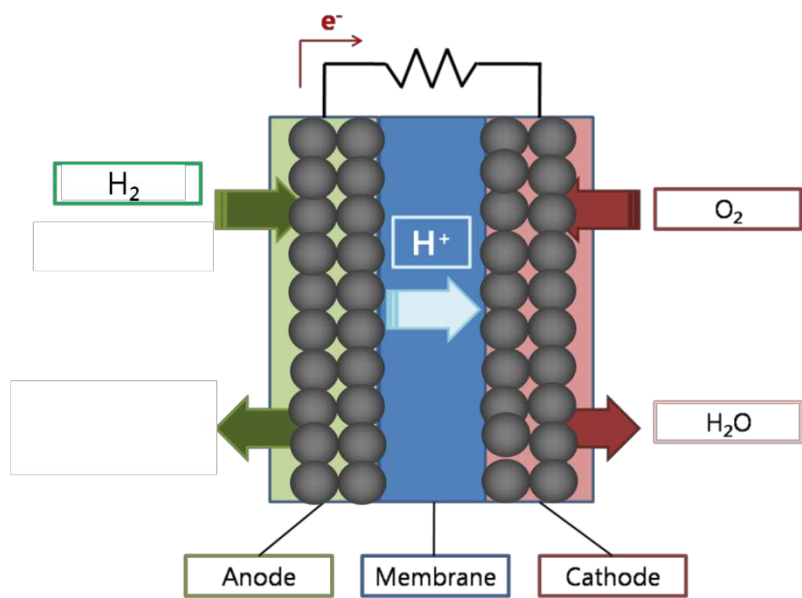


Fig. 1.2 Scheme of PEMFC operation

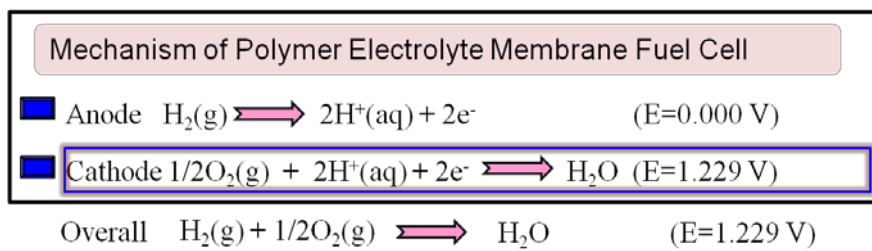


Fig. 1.3 Overall reaction of anode and cathode reaction in PEMFC

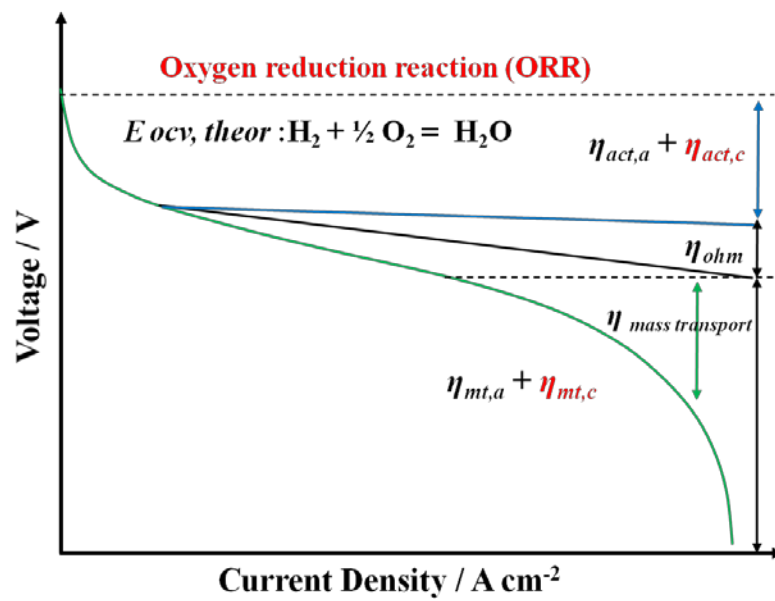


Fig. 1.4 Polarization curve of anode and cathode reaction in PEMFC

1.2 Concepts of Study

Over the past two decades nanocatalysts have attracted extensive amount of interest as the key to resolve the hardship of commercialization of fuel cells. In first stage of nanocatalysts study it was focused forging high catalytic activity by tuning the surface structure of the nanocatalysts, size and shape of the nanocatalysts, and alloying different metals [4-20]. The enhanced ORR activity of Pt skin on single crystal substrates had been suggested by Adzic's group applying various Pt skin electrocatalyst which was prepared using Cu displacement reaction. The Pt skin catalyst showed 10-fold mass activity compared to that of Pt nanoparticle catalyst. Norskov's group has researched theoretically the effect of substrate on the electronic structure and electrocatalytic properties of Pt skin catalyst. They proposed a "d-band model" which describes the ORR activity of Pt skin catalysts using a one parameter, average energy level of filled 5d-band in Pt skin layer.

As a result, satisfactory catalytic activity was obtained; however, in contrast to evolvement of catalytic activity insufficient of improvement was found for the stability. Resolving the insufficient stability of the nanocatalysts may play a role as an engine to boost up the nanocatalysts study to a second stage.

Many researchers did empirical and theoretical study to reconcile the high activity and high stability of the nanocatalysts.[21-23] In recent study, the enhanced stability of PtNi tuning the composition and surface morphology was reported by Markovic et al.[24] The computational screening of Pt coated on various core materials was scrutinized to select

the suitable nanocatalysts for activity and stability.[25] Kim et al. did a study on a highly porous structured Pt that possess high stability and reasonable catalytic activity for ORR.[26]

In this thesis, the effect of structure enhancement on the nanocatalysts for ORR activity was investigated using carbon supported nanostructure catalysts which have different nanostructure and heterogeneous atoms core decorated by Pt effect in the catalyst surfaces. The structure modifications were conducted in four different ways: 1) synthesis of 20 nm Pt cluster formed with small 5 nm sized Pt nanoparticles, 2) urchin like structured PtNi with formed with 1-D rod 3) post thermal treatment of Pd-Fe alloy nanoparticles under air and H₂ gas which led to Pd rich surface Pd-Fe core compositions with high alloying degree 4) decorating Pd-Fe alloy nanoparticles with Pt applying hydroquinone method.

1.3 References

1. R.P. O'Hayre, S.-W. Cha, W. Colella, F.B. Prinz, FUEL CELL FUNDAMENTALS, *John Wiley & Sons, New York*, **2006**.
2. F. Barbir, PEM Fuel Cells: Theory and Practice, Elsevier Inc., London, 2005.
3. A. Dhanda, H. Pitsch, R. O'Hayre, "Diffusion impedance element model for the triple phase boundary", *J. Electrochem. Soc.* **2011**, 158, B877.
4. U. A. Paulus, A. Wokaun, G. G. Scherer, T. J. Schmidt, V. Stamenkovic, V. Radmilovic, N. M. Markovic, P. N. Ross, "Oxygen reduction on carbon-supported Pt–Ni and Pt–Co alloy catalysts", *J. Phys. Chem. B* **2002**, 106, 4181.
5. K. J. J. Mayrhofer,* B. B. Blizanac, M. Arenz, V. R. Stamenkovic, P. N. Ross, N. M. Markovic, "The Impact of geometric and surface electronic properties of Pt-catalysts on the particle size effect in electrocatalysis", *J. Phys. Chem. B* **2005**, 109, 14433.
6. I. E. L. Stephens, A. S. Bondarenko, U. Grønbjerg, J. Rossmeisl, I. Chorkendorff, "Understanding the electrocatalysis of oxygen reduction on platinum and its alloys", *Energy Environ. Sci.* **2012**, 5, 6744.
7. Hong Yang, "Platinum-based electrocatalysts with core–shell nanostructures", *Angew. Chem. Int. Ed.* **2011**, 50, 2674.
8. K. J.J. Mayrhofer, V. Juhart, K. Hartl, M. Hanzlik, M. Arenz, "Adsorbate-induced surface segregation for core–shell nanocatalysts", *Angew. Chem. Int. Ed.* **2009**, 48, 3529.
9. T. K. Sau, A. L. Rogach, "Nonspherical noble metal nanoparticles: colloid-chemical synthesis and morphology control", *Adv. Mater.* **2010**, 22, 1781.
10. J. Wu, J. Zhang, Z. Peng, S. Yang, F. T. Wagner, H. Yang, "Truncated octahedral Pt₃Ni oxygen reduction reaction electrocatalysts", *J. AM. Chem. Soc.* **2010**, 132, 4984.
11. Y. Chen, Z. Liang, F. Yang, Y. Liu, S. Chen, "Ni–Pt core–shell nanoparticles as oxygen reduction electrocatalysts: effect of Pt shell coverage", *J. Phys. Chem. C* **2011**, 115, 24073.
12. J. R. Kitchin, J. K. Nørskov, M. A. Barteau, J.G. Chen, "Role of strain and ligand effects in the modification of the electronic and chemical properties of bimetallic surfaces", *Phys. Rev. Lett.* **2004**, 93, 156801.
13. M. P. Hyman, J. W. Medlin, "Effects of electronic structure modifications on the adsorption of oxygen reduction reaction intermediates on model Pt(111)-alloy

- surfaces", *J. Phys. Chem. C* **2007**, 111, 17052.
14. V. Stamenkovic, T. J. Schmidt, P. N. Ross, N. M. Markovic, "Surface segregation effects in electrocatalysis: kinetics of oxygen reduction reaction on polycrystalline Pt₃Ni alloy surfaces", *J. Anal. Chem.* **2003**, 554-555, 191.
 15. C. Wang, H. Daimon, T. Onodera, T. Koda, S. Sun, "A general approach to the size- and shape-controlled synthesis of platinum nanoparticles and their catalytic reduction of oxygen", *Angew. Chem. Int. Ed.* **2008**, 47, 3588.
 16. V. Tripkovic, E. Skúlasona, S. Siahrostamia, J. K. Nørskov, J. Rossmeisl, "The oxygen reduction reaction mechanism on Pt(111) from density functional theory calculations", *Electrochim. Acta* **2010**, 55, 7975.
 17. V. R. Stamenkovic, B. Fowler, B. S. Mun, G. Wang, P. N. Ross, C. A. Lucas, N. M. Markovic, "Improved oxygen reduction activity on Pt₃Ni(111) via increased surface site availability", *Science* **2007**, 315, 493.
 18. J. X. Wang, N. M. Markovic, R. R. Adzic, "Kinetic analysis of oxygen reduction on Pt(111) in acid solutions: intrinsic kinetic parameters and anion adsorption effects", *J. Phys. Chem. B* **2004**, 108, 4127.
 19. V. Stamenkovic, N. M. Markovic, P.N. Ross Jr., "Structure-relationships in electrocatalysis: oxygen reduction and hydrogen oxidation reactions on Pt(111) and Pt(100) in solutions containing chloride ions", *J. Anal. Chem.* **2001**, 500, 44.
 20. N. Markovic, H. Gasteiger, P. N. Ross, "Kinetics of oxygen reduction on Pt(hkl) electrodes: implications for the crystallite size effect with supported Pt electrocatalysts", *J. Electrochem. Soc.* **1997**, 144, 1591.
 21. C. Wang, M. Chi, D. Li, D. Strmcnik, D. Vliet, G. Wang, V. Komanicky, K.-C. Chang, A. P. Paulikas, D. Tripkovic, J. Pearson, K. L. More, N. M. Markovic, V. R. Stamenkovic, "Design and synthesis of bimetallic electrocatalyst with multilayered Pt-skin surfaces", *J. Am. Chem. Soc.* **2011**, 133, 14396.
 22. S. Chen, W. Sheng, N. Yabuuchi, P. J. Ferreira, L. F. Allard, Y. Shao-Horn, "Origin of oxygen reduction reaction activity on "Pt₃Co" nanoparticles: atomically resolved chemical compositions and structures", *J. Phys. Chem. C* **2009**, 113, 1109.
 23. D. F. Vliet, C. Wang, D. Li, A. P. Paulikas, J. Greeley, R. B. Rankin, D. Strmcnik, D. Tripkovic, N. M. Markovic, V. R. Stamenkovic, "Unique electrochemical adsorption properties of Pt-Skin surfaces", *Angew. Chem. Int. Ed.* **2012**, 51, 3139.
 24. D.F. Vliet, C. Wang, D. Tripkovic, D. Strmcnik, X.F. Zhang, M.K. Debe, R. T. Atanasoski, N.M. Markovic, V.R. Stamenkovic, " Mesostructured thin films as electrocatalysts with tunable composition and surface morphology", *Nature Materials* **2012**, 11, 1051.

25. S.J. Hwang, S.J. Yoo, J. Shin, Y.-H. Cho, J.H. Jang, E. Cho, Y.-E. Sung, S.W. Nam, T.-H. Lim, S.-C. Lee, S.-K. Kim, "Supported core@shell electrocatalysts for fuel cell: close encounter with reality" *Scientific Reports* **2013**, 3, 1309.
26. D.-S. Kim, C. Kim, J.-K. Kim, J.-H. Kim, H.-H. Chun, H. Lee, Y.-T. Kim, "Enhanced electrocatalytic performance due to anomalous compressive strain and superior electron retention properties of highly porous Pt nanoparticles" *J. Catalysis* **2012**, 291, 69.

Chapter 2

Experimental

2.1 Catalyst preparation

2.1.1 Synthesis of Pt cluster

Materials. Platinum acetylacetonate ($\text{Pt}(\text{acac})_2$) was purchased from Strem. 1-Adamantanecarboxylic acid (ACA, 99%), 1,2-hexadecanediol (HDD), 1-hexadecylamine (HDA, 90%), diphenyl ether (DPE), were purchased from Aldrich. All chemicals and reagents were used without further purification.

In a standard synthesis, 22.5 mg of ACA (0.125 mmol) and 0.5 g of HDA (2.05 mmol) were dissolved in 5 mL of DPE. After an sufficient mixing with the magnetic stirring 25 mg of $\text{Pt}(\text{acac})_2$ (0.063 mmol), and 0.4 g of HDD (1.55 mmol) were poured into the mixture under a vigorous stirring. The mixture solution was transferred to a three neck flask and was heated to 160 °C at a heating rate of 4 °C/min under Ar atmosphere and kept at this temperature for 1 hr. The mixture solution was cooled to room temperature after the reaction and the products were precipitated by centrifugation after adding ethanol. After the reaction the mixture solution was cooled and the products were

precipitated by centrifugation after adding ethanol and dried in a vacuum desiccator for over a night. The Pt cluster nanostructures were loaded on the carbon using hexane. 300 ml of hexane was poured into the beaker with the following step of putting in the optimum amount of carbon black (Vulcan XC-72R) into the solvent. The mixture was stirred for 30 min and sonicated for 30 min to achieve uniform dispersion of carbon. After the sonication Pt cluster nanostructures were plunged into the mixture and sonicated for 1 hr 30 min. Subsequently, the mixture was removed from the sonicator and placed onto the magnetic stirrer for 12 hr stirring.

2.1.2 Urchin like PtNi nanostructures

Materials. Platinum acetylacetonate ($\text{Pt}(\text{acac})_2$) Nickel acetylacetonate ($\text{Ni}(\text{acac})_2$) were purchased from Strem. 1-Adamantanecarboxylic acid (ACA, 99%), 1,2-hexadecanediol (HDD), 1-hexadecylamine (HDA, 90%), diphenyl ether (DPE), were purchased from Aldrich. All chemicals and reagents were used without further purification.

The Pt-Ni nanostructures were synthesized by using heat-up process of a mixture solution containing $\text{Pt}(\text{acac})_2$, $\text{Ni}(\text{acac})_2$, hexadecylamine (HDA), 1-adamantane carboxylic acid (1-ACA). 22.5 mg of ACA (0.125 mmol) and 0.5 g of HDA (2.05 mmol) were dissolved in 5 mL of DPE. After an sufficient mixing with the magnetic stirring 25

mg of Pt(acac)₂ (0.063 mmol), and 0.4 g of HDD (1.55 mmol) were poured into the mixture under a vigorous stirring. The mixture solution was heated at 240 °C, and aged for 30 min. After the reaction the mixture solution was cooled to room temperature and the products were precipitated by centrifugation after adding ethanol and dried in a vacuum desiccator for over a night. The urchin like PtNi nanostructures were loaded on the carbon using hexane. 300 ml of hexane was poured into the beaker with the following step of putting in the optimum amount of carbon black (Vulcan XC-72R) in to the solvent. The mixture was stirred for 30 min and sonicated for 30 min to achieve uniform dispersion of carbon. After the sonication urchin like PtNi nanostructures were plunged into the mixture and sonicated for 1hr 30 min. Subsequently, the mixture was removed from the sonicator and placed onto the magnetic stirrer for 12 hr stirring.

2.1.3 Synthesis of PdFe nanoparticles

Carbon supported Pd-Fe (40 wt %) alloy nanoparticles were prepared via two-step reduction method. Synthesizing Pd nanoparticles with oleylamine has previously been reported in detail and took an advantage of that [27]. Pd-Fe alloy nanoparticles were synthesized by polyol reducing method using 1,2-propanediol as solvent and reducing agent. 0.15 g of carbon black (Vulcan XC-72R) and 0.36 ml of oleylamine (1.58×10^{-3} mol), as a stabilizer, were dispersed in 1,2-propanediol (200 ml) and stirred for 1 hr and sonicated for 30 min. In sequence, certain amounts of Palladium (II) acetylacetonate

and Fe (II) acetylacetonate, as precursors, were added to the mixture solution and kept in stirring condition for 6 hr. After sonication for 3 min, the solution was heated to 110 °C in a three neck flask under an Ar atmosphere and maintained at the temperature for 1 hr to withdraw residuary water. 0.2270 g of NaBH₄ (0.012 mol) was added to the heated solution under vigorous stirring circumstances and held it for 1 hr to reduce the reduction energy gap between Pd and Fe precursors and to initiate the nucleation. The mixture was heated up to 165 °C and remained at this temperature for 2 hr for complete reduction of two precursors. After cooling to room temperature, the solution was filtered, washed with ethanol, and dried in a vacuum desiccator.

2.1.4 Pd-rich PdFe alloyed nanoparticles by post treatment

In order to make carbon supported Pd rich PdFe nanoparticles post treatment method has been used. Pristine PdFe catalysts with atomic ratios of Pd to Fe varying from 3:1, 1:1, and 1:3 were heated in a tube furnace at 200 °C in air for 1 hr, and heated up to 300 °C for 3hr and to 500 °C for 2hr. After the heat process samples stayed inside the furnace for 12 hr under 5 vol % H₂ in Ar. Subsequently, the samples were cooled down to room temperature under Ar. The resulting post heat treated ASP Pd_xFe is denoted as HT Pd_x-Fe.

2.1.5 Pt decorated on PdFe core nanoparticles

PdFe-core nanoparticles decorated with Pt were prepared using a redox chemistry of hydroquinone/quinine (HQ/Q) in a protic solvent (ethanol, anhydrous). PdFe-core

catalysts were mixed in a 100 ml of ethanol for 3hr to obtain a homogeneous state for the decoration of Pt. HQ and PtCl₄ was dissolved in an each vial which contained 20 ml of ethanol. Subsequently, the HQ solution and PtCl₄ solution was poured inside the PdFe-core solution and deaerated for 1hr with Ar flow in room temperature. After the deaeration the mixture was transferred to a three neck flask and heated up to 70 °C and stayed at that temperature for 2 hr. Finally, the mixture solution was cooled to room temperature under Ar. The mixture solution was filtered, washed with ethanol, and dried in a vaccum desiccator. As a result Pt/PdFe atomic ratios of PdFe@Pt were 0.1/1, 0.5/1, and 1/1.

2.2 Physical and electronic structure measurements

2.2.1 X-ray diffraction

X-ray diffraction (XRD) is a well known relatively easy, non-destructive, and quick analyzing technique in examining the internal structure of materials. The principle of diffraction is related with the phase relations between two or more X-ray waves. For example, X-ray diffraction of a crystal, an interaction between the incident X-ray and the crystalline planes which satisfy Bragg condition make constructive interference.

$$n\lambda = 2d \sin \theta$$

In above equation, n means the order of diffraction (natural number), λ indicates the wave length of the X-ray, d is the distance between crystalline planes, and θ is incident angle of X-ray [27-29]. In θ -2 θ scan mode, crystallographic structure of materials are depicted as crystal structure and lattice parameter. Imperfectness of crystal make line broadening of diffraction peak which is commonly represented by full with half maxima (FWMH). As the finite size of crystal gave increase of FWHM which follows the Scherrer equation, the crystalline size of nanoparticles can be calculated form the line broadening of XRD peak.

$$d = \frac{0.94 \times \lambda \kappa_{\alpha 1}}{\beta_{(2\theta)} \cos \theta_{\max}}$$

Where, d is the mean crystalline size, $\lambda \kappa_{\alpha 1}$ is the wave length of X-ray, θ_{\max} indicates the angle at the maximum, and $\beta_{2\theta}$ is the width of the peak at half height. In this thesis a powder X-ray diffraction (XRD) patterns were recorded by Rigaku D/MAX 2500 operated with a Cu Ka source ($\lambda = 1.541 \text{ \AA}$) at 40 kV and 200 mA. The angle extended from 20° to 80° and the scan rate was 2° per minute.

2.2.2 Transmission electron microscopy

Transmission electron microscopy (TEM) is one of the most efficient and resourceful tool for the characterization of morphology and spatial range of nanocatalysts. Nano-sized materials can be analyzed by under large magnifications, high elemental resolution with a scanning probe apparatus. In this thesis, the particle distribution and size of the nanocatalysts were analyzed by high resolution-transmission electron microscope (HR-TEM). TEM images were taken by using a 2100F, JEOL 2010, and TEKNI F-20 electron microscope for TEM and scanning transmission electron microscopic images, respectively. The samples were prepared by dispersing a small amount of nanocatalyst powder in a volatile solvent (ethanol) subsequently with ultrasonication. Then, the catalyst/ethanol mixture was dropped onto a holey carbon film on 200 mesh copper grid and dried in oven at 60 °C.

2.2.3 X-ray absorption spectroscopy (XAS)

XAS is a widely used technique usually performed at synchrotron radiation sources, which provide intense and tunable various X-ray beams. Through this XAS measurement it is favorable to determine the local geometric and electronic structure of the material. XAS is a data that involves excitation of core electrons by photon energy injected from ring source. The principal quantum numbers $n=1, 2,$ and $3,$ correspond to the K-, L-, and M- edges, respectively. The excitation of $1s$ electron refers to K-edge and $2s$ or $2p$ excitation refers to L-edge. XAS data is divided into three regions 1) pre edge 2) rising edge 3) extended X-ray absorption fine structure (EXAFS). Pre edge region is called X-

ray absorption near-edge structure (XANES) and corresponds to oxidation state and chemical environment of absorbing element. On the other hand, EXAFS region is sensitive to the radial distribution of electron density and is useful to analyze quantitatively the bond length and coordination number. Pt L_{III} edge and Ni K edge of Pt cluster and urchin like PtNi were obtained at the Pohang Light Source (PLS) using the 8C and 10C beamline with a ring current of 120-170 mA at 2.5 GeV (Fig. 2.3). In case of PdFe Pd K edge was obtained with the light source using 7D. Before the measurements, X-ray energy was calibrated to the Pt L_{III} edge energy using Pt foil as a reference and for Pd and Ni K edge it was Pd foil and Ni foil, respectively. XAS spectra were collected using a fluorescence detector in air ambient. The XAS data were fitted with ATHENA and ARTEMIS software to obtain the absorbance of the material. The background removal of XANES spectra were the first step of the fitting. Fitting pre-edge data to a Victoreen-type formula over a range of 200-40 eV below the edge was followed by extrapolation over the energy range of interest and subtraction from the data. After removal of all backgrounds, second step was plotting second derivatives calculated from inflection points of data from the reference channel. Third step, the normalization value was chosen as the absorbance at the inflection point of one extended X-ray absorption fine structure (EXAFS) oscillation. The spectra were thus normalized by dividing each datum point by the normalization value.

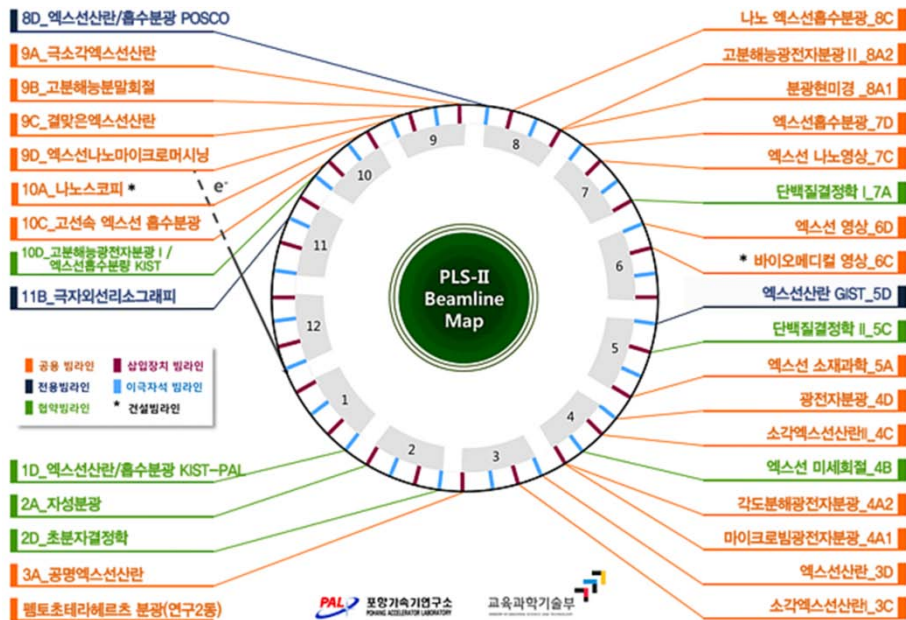


Fig. 2.1 Beamline map in the PAL. From the webpage, <http://pal.postech.ac.kr>.

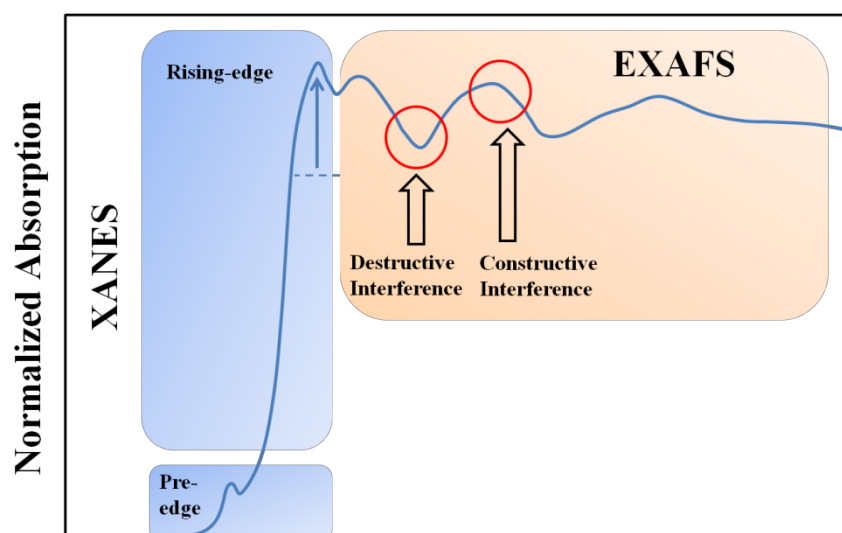


Fig. 2.2 Three main regions of X-ray absorption spectroscopy

2.3 Electrochemical characterizations

2.3.1 Cyclic electrode voltammetry and Rotating disk

Cyclic voltammetry (CV) is an electrochemical measurement that measures the changes in the cathodic and anodic current with gradual potential increase. For cathodic and anodic scan when the potential reaches a set potential the working potential ramp is inverted. In CV plot vertical axis is the current of working electrode and horizontal axis is applied voltage. To prepare a catalyst ink for working electrode the catalyst ink slurry was prepared by mixing 0.01 g of carbon supported alloy nanoparticles with 20 μL DI water, 60 μL 5 wt% Nafion solution (Aldrich Chem. Co) as a binding material, and 700 μL isopropyl alcohol (IPA). After mixing and ultrasonication, 7 μL of ink slurry was pipetted and dropped onto a glassy carbon substrate (geometric surface area 0.196 cm^2). Electrochemical measurements were carried out in an Autolab potentiostat (PGSTAT101) using a conventional three-electrode electrochemical cell comprised of a glassy carbon working electrode, a platinum wire counter electrode, and a saturated calomel reference electrode (SCE). All electrochemical measurements are quoted with respect to reversible hydrogen electrode (RHE) and were conducted at 293 K. ORR was measured by rotating disk electrode (RDE) technique. RDE technique is a system for which the hydrodynamic equations and convective-diffusion equation have been used for steady state. The RDE is consisted of a disk of electrode, glassy carbon or platinum, in a insulating material. ORR

polarization curves were obtained using a RDE 1,600 rpm, with scanning from -0.094 to 0.756 V vs SCE at 5 mV s^{-1} in 0.1 M HClO_4 under an O_2 flow.

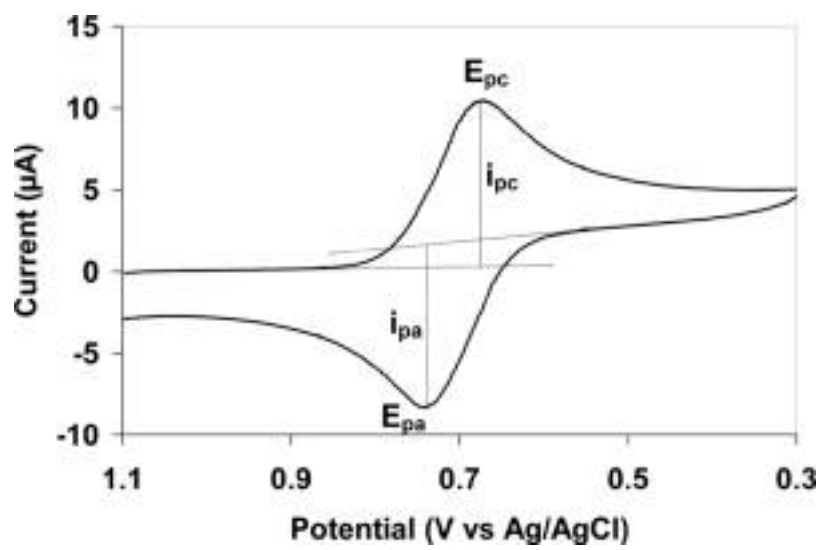


Fig. 2.3 Profile of cyclic voltammetry

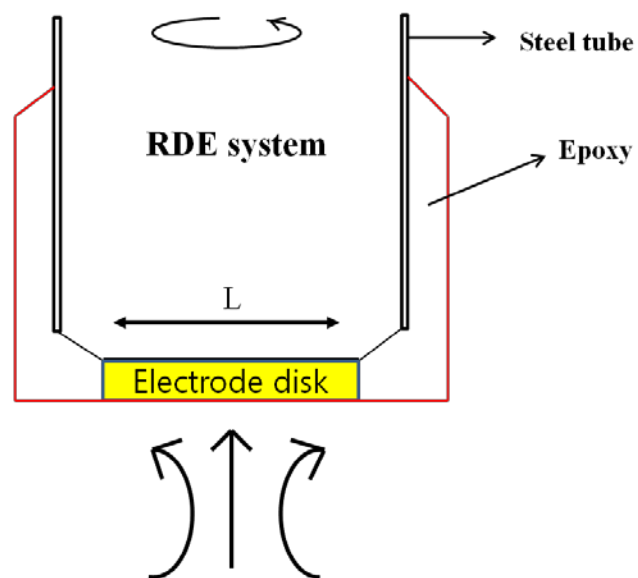


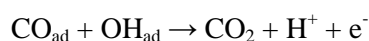
Fig. 2.4 Scheme of rotating disk electrode

2.3.2 CO electrooxidation

The mechanism of electrochemical oxidation of CO is governed by Langmuir-Hinshelwood model (Fig 2.5). Reaction of CO electrochemical oxidation begins with the elementary reaction steps of water activation



Where OH_{ad} represents to adsorbed oxide species. Adsorbed CO oxidation follows the equation



The onset of CO_{ad} oxidation for CO adlayer can be explained from displacing of H_{ad} during the CO adsorption. Oxidation of remaining H_{ad} works as a CO-free site which induces the oxidation of CO_{ad} [30-32].

CO displacement experiments, described in detail by Clavilier et al. allow the potential of zero total charge (PZTC) to be calculated. After cyclic voltammetry test in Ar-purged 0.1 M HClO_4 (aq.), CO (99.99 % purity) was flowed into the electrolyte for 10 min at a constant potential (-0.044 V vs SCE) and the current generated by displacing the existing adsorbates with CO_{ads} was then recorded. After saturation of PdFe surface by CO_{ads} , excess CO_{bulk} was eliminated from all parts of the cell using an Ar flow for 30 min. Cyclic voltammetry of oxidation were then obtained. To calculate the PZTC, the CO displacement charge was subtracted from the H_{upd} charge

that was integrated from the CO dosing potential. Because PZTC is the potential at which an excess charge on the electrode is zero, it is the potential at which the subtraction equals to zero.

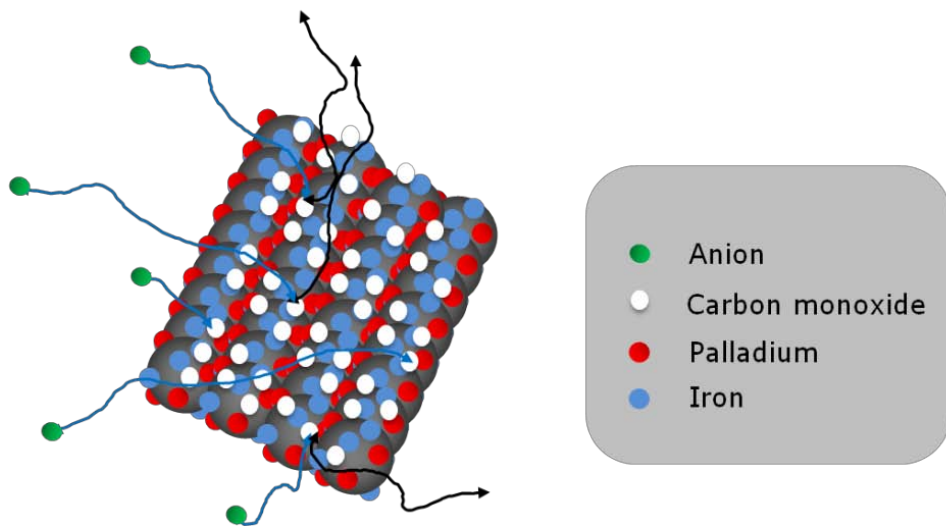


Fig. 2.5 Scheme of Langmuir-Hinshelwood mechanism

2.4 References

27. E. Antolini, F. Cardellini, "Formation of carbon supported PtRu alloys: an XRD analysis", *J. Alloy Com.*, **2001**, 315, 118.
28. T. Lopes, E. Antolini, E.R. Gonzalez, "Carbon supported Pt-Pd as an ethanol tolerant oxygen reduction electrocatalysts for direct ethanol fuel cells", *Int. J. Hydrogen Energ.* **2008**, 33, 5563.
29. E. Antolini, L. Giorgi, F. Cardellini, E. Passalacqua, "Physical and morphological characteristics and electrochemical behavior in fuel cells of PtRu/C catalysts", *J. Solid State Electrochem.* **2001**, 5, 131.
30. A.V. Petukhov, " Effect of molecular mobility on kinetics of an electrochemical Langmuir-Hinshelwood reaction", *Chem. Phys. Lett.* **1997**, 277, 539.
31. P. Inkaew, C. Korzeniewski, "Kinetic studies of adsorbed CO electrochemical oxidation on Pt(335) at full and sub-saturation coverages", *Phys. Chem. Chem. Phys.*, **2008**, 10, 3655
32. A.R. Kucernak, G.J. Offer, "The role of adsorbed hydroxyl species in the electrocatalytic carbon monoxide oxidation reaction on platinum", *Phys. Chem. Chem. Phys.* **2008**, 10, 3699

Chapter 3

Results and discussion

3.1 Cluster Shaped Nanocatalysts

3.1.1 Pt nanocluster structure

The Proton exchange membrane fuel cells (PEMFCs) are the most promising renewable energy technologies to solve the exhaustion of fossil fuel and oil because of the advantages such as low operating temperature, high power density, low production of byproducts leading to the pollution and climate change induced by fossil fuel combustion. Until now, platinum group metal (PGM)-based materials are a dominant class of electrocatalyst for efficient electrochemical energy conversion devices. However, commercialization of PEMFC's has been hindered due to the slow kinetics of the oxygen reduction reaction (ORR), which, in turn, decreases the overall performance of PEMFCs. In addition, the scarcity and high cost of Pt metal drives up the cost of manufacturing fuel cells. Therefore, a majority of fuel cell research focuses on searching for catalysts not only reduce the amount of Pt used but also enhances the catalytic activity and stability of the ORR.

Pt dissolution follows three reaction steps [1]:



In order to prevent the Pt catalyst dissolution each steps reaction has to be hindered. In order to reconcile these requirements, several approaches have been developed, such as making nanostructures to increase the surface-to-volume ratio, controlling the shapes to increase the number of active sites on Pt nanoparticles, and alloying two or more non-precious metals into the nanostructures [2-5]. The activity and the stability of the Pt can be tailored by regulating the shape and morphology due to the edge and corner atoms. Therefore, many scientists have studied on the synthesis of Pt with tetrahedral, multiarmed nanostar, and multioctahedral shape. Lim et al. reported that highly faceted multioctahedral Pt nanocrystals consisted of interconnected arms with quasi-octahedral shape have a substantial amount of edge, corner, and surface stepped atoms on the catalyst surfaces [6-7]. As a result, it was evident that high ratio between (111) and (100) exhibited higher ORR specific activity. Kim et al. did an investigation on the urchin like highly porous Pt with high proportion of surface atoms [1]. In case of urchin like Pt, the (111) and (110) facets played a pivotal role to improve electron retention and to decrease the proportion of low-coordinated sites, which enhanced the stability against Pt dissolution. There are other ways to improve the stability of the nanocatalysts that are used for ORR catalyst. Adzic et al. improved the stability of Pt by depositing Au cluster

on to the Pt [3]. In the paper, they explained because of the efficient spillover of H_2O_2 from Au clusters to the surrounding Pt atoms confronts additional reduction to H_2O which enhances the stability.

Here we would like to report a 20-30 nm Pt nanostructure that is constructed with small Pt nanoparticles (5 nm), which is defined as a cluster, which has high oxygen reduction reaction activity and stability. Pt cluster synthesis method applies HDD as a reducing agent to control the reduction of the $\text{Pt}(\text{acac})_2$ and long-chain amine HDA as a main capping agent.

3.1.2 Crystalline and surface structure of Pt cluster

The chemical analysis of Pt cluster was conducted by inductively coupled plasma-atomic emission spectroscopy (ICP-AES). The weight percent of Pt cluster (20.4 wt %) loaded on carbon was confirmed by elemental analysis. The lattice structure and the morphology of the Pt cluster were confirmed from the high resolution TEM images. As shown in Fig. 3.1, the Pt cluster nanostructures are formed with small nanoparticles that have 5 nm of average size which is in good agreement with the XRD result (5.40 nm). Furthermore, Fourier transformed dark-field image corroborated reciprocal lattice points to identify the facets of the Pt cluster. It turned out that Pt cluster is dominantly consisted with (111) and (110) facets. The average particle size of Pt cluster and commercial Pt was calculated by using Scherrer's equation [8-10];

$$L = \frac{K\lambda}{B \cos \theta}$$

Where, L is the average particle size, K is the constant which refers to the shape of crystals, λ is the wave length of radiation, B is the FWHM (in radians) of the peak, and θ is the diffraction angle of the crystal plane. There was no peak difference between Pt cluster and commercial Pt (Fig. 3.2). The (220) peak was chosen to evaluate the particle size and shift of the peak. Because it is obvious that (220) peak does not have any neighboring peaks such as a carbon peak. The particle size for Pt cluster and commercial Pt were 5.40 nm and 3.77 nm, respectively. In other words, Pt cluster is a large structure that is formed with small nanoparticles. Therefore, the physical and chemical characteristics of Pt cluster can be interpreted as a 5 nm size Pt nanoparticles. Additionally, the (111) peak area / (220) peak area ratio was 3.90 and 2.73 for Pt cluster and commercial Pt, respectively. The (111) peak area / (220) peak area ratio supports, Pt cluster has dominant (111) facets in comparison with that of commercial Pt. The stability of morphology and crystallinity were confirmed by the TEM images that have been obtained after 10,000 cycles of ADT test (Fig. 3.3). There was no agglomeration between the Pt clusters and no destruction of (111) facets of Pt cluster.

3.1.3 Electrochemical characterization of Pt cluster

Electrochemical measurements were performed in a room temperature (20 °C) controlled electrolyte with a conventional three electrode electrochemical cell comprised

of a glassy carbon working electrode, a platinum wire counter electrode, and a saturated calomel reference electrode (SCE). The reference electrode potential was corrected to a reversible hydrogen electrode (RHE). Catalyst ink was prepared with 5 wt % Nafion solution, 2-propanol, and 0.01 g of Pt cluster catalyst. The catalyst ink (3 μ l) was dropped onto the working electrode and dried at 60 °C oven for 15 min.

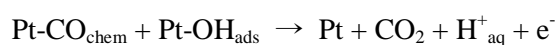
Pre cycling of the catalyst was taken in an Ar saturated 0.1 M HClO₄ electrolyte before cyclic voltammogram (CV) measurement. The potential range, scan rate, and cycling number of the pre cycling were 0 V to 0.4 V, 100 mV s⁻¹, and 30 cycles, respectively. After the pre cycling, when the double layer is stable and the surface cleaning is completed, cyclic voltammogram measurement was conducted with a scan rate of 20 mV s⁻¹ for 3 cycles. CO electrooxidation was performed in the 0.1 M HClO₄ electrolyte, saturated with 10 % CO at the adsorption electrode potential of 0.01 V to define the specific surface domains and sites. In order to survey the ORR activity of the Pt cluster the ORR measurement was conducted on the rotating disk electrode (RDE). ORR polarization curve was obtained in an O₂ saturated 0.1 M HClO₄ electrolyte at a scan rate of 5 mV s⁻¹ and at a rotating rate of 1600 rpm. ADT test condition was identical with the US Department of Energy recommended for the ADT test. The total number of the cycle was 10,000 cycles and the ADT potential range was from 0.6 V to 1.1 V.

Ross et al. elucidated that three different levels of crystallinity affects the adsorption of anion in an acid medium and Pt (111) facet shows the best ORR activity in perchloric acid [11]. Fig. 3.4 shows the difference of H₂ adsorption and desorption of Pt cluster and

commercial Pt. In case of commercial Pt (20 wt %) it is obvious that H₂ adsorption peak has been formed. In contrast, Pt cluster manifested potential ranging from 0.05 V to 0.4 V. For commercial Pt, the anodic potential range between 0.7 V and 1.0 V there is a distinct peak indicating OH oxidation. This phenomenon is observed for a catalyst with a small particle size, which in terms of low-coordinated sites such as edge, kink, and corner sites. In contrast, Pt cluster OH formation is shifted to a higher potential

As shown in Fig. 3.5, the ORR polarization curves of Pt cluster and commercial Pt, the half wave potential ($E_{1/2}$) of Pt cluster is (0.92 V) located 0.03 V higher than that of the commercial Pt (0.89 V), construing that ordered single crystalline phase, small proportion of low-coordinated sites, and lattice contraction gained by the porous structure are the factors for the ORR enhancement.

Jerkiewicz et al. studied on the correlation between CO monolayer oxidation and Pt nanoparticle surface structure with cubic, octahedral, and cuboctahedral. The desorption of CO_{chem} process follows a Langmuir-Hinshelwood mechanism;



To intensively study the surface structure of the Pt cluster, CO oxidation measurement was conducted in the perchloric acid. As shown in Fig. 3.6 the pre-ignition peak around 0.7 V and 0.85 V was detected for Pt cluster and commercial Pt. In case of Pt cluster the peak at 0.72 V is attributed to (111) and (100) facets. These relatively ordered facets

verified from the CO oxidation correspond to the increment of Pt cluster's crystallinity. In addition, the unique structural property of Pt cluster affected the d-band center of Pt which changes the adsorption energy between Pt and oxygenated species.

The most important research result from Pt cluster was retention of the stability even after 10,000 cycles of cyclic voltammetry. The cyclic voltammogram of Pt cluster and commercial Pt before and after ADT test is well depicted in Fig. 3.7. The initial ESA and after 10,000 cycles of ADT ESA of Pt cluster were $4.176 \text{ m}^2 \text{ g}^{-1}$ and $4.04 \text{ m}^2 \text{ g}^{-1}$, respectively. The total percentage of the decrement was 4.11 %.

In case for commercial Pt the initial ESA and after 10,000 cycles of ADT ESA were $68.46 \text{ m}^2 \text{ g}^{-1}$ and $23.04 \text{ m}^2 \text{ g}^{-1}$. The total percentage of the decrement for commercial Pt was almost 18 times higher than Pt cluster (63.64 %). The reason for this high stability can be explained from several factors certified from the surface structure and electrochemical analysis. Sun et al. synthesized 1-D morphology Pt catalyst with (111) facet growth [13]. They did 4000 cycles of the ADT test with their 1-D morphology Pt catalyst and commercial Pt samples. 1-D morphology Pt catalyst exhibited higher stability than commercial Pt due to the (111) facet oriented 1-D multiarms. This theory could also be applied to Pt cluster for the enhancement of stability. Pt cluster crystallinity dominantly oriented with (111) was confirmed by the TEM images, CO oxidation, and XRD.

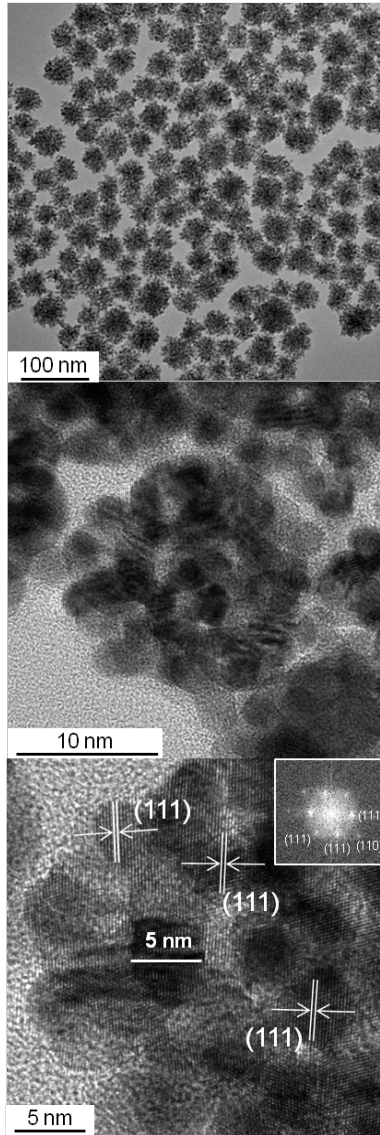


Fig. 3.1 TEM images of Pt cluster.

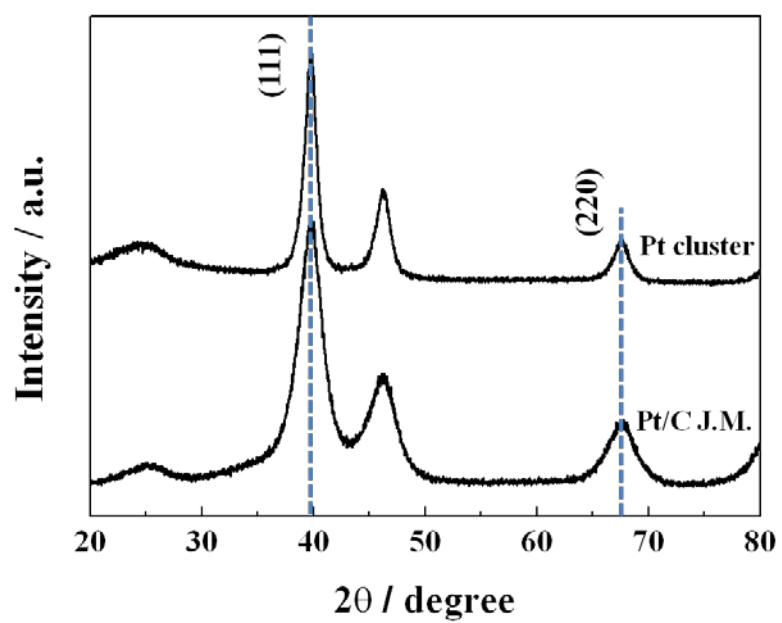


Fig. 3.2 XRD of Pt cluster and commercial Pt.

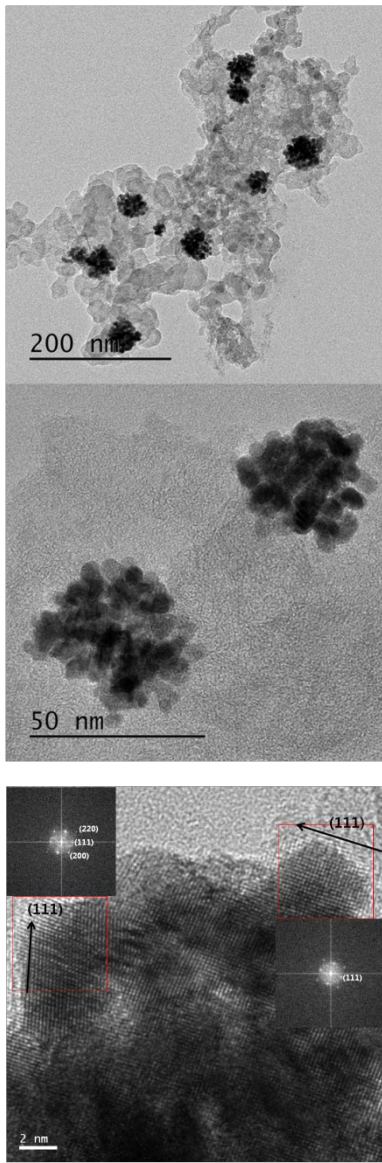


Fig. 3.3 TEM images of Pt cluster after 10,000 cycles ADT test

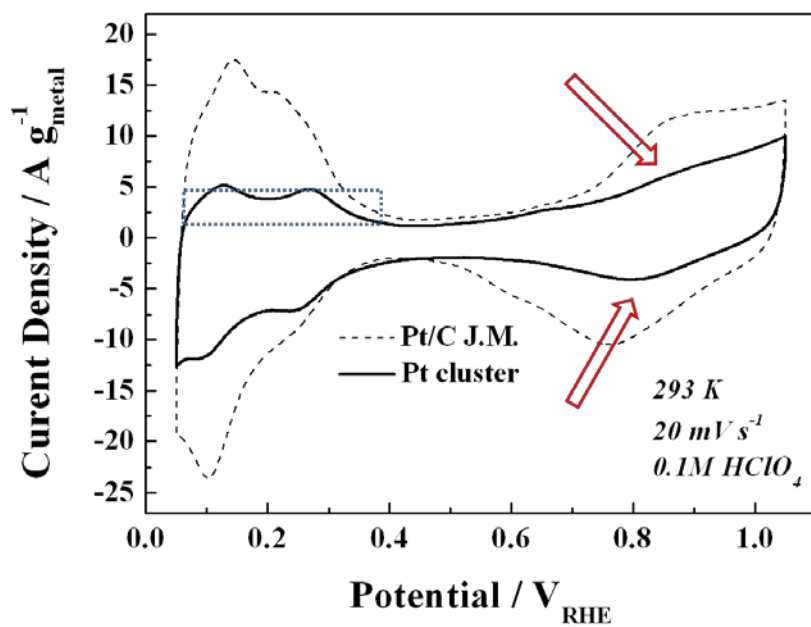


Fig. 3.4 Cyclic voltammetry of Pt cluster and Pt/C J.M.

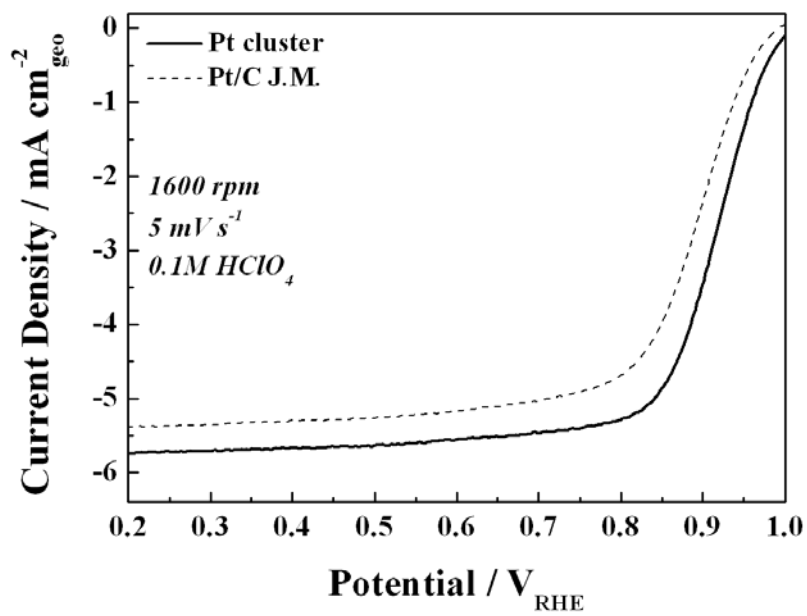


Fig. 3.5 ORR polarization curve of Pt cluster and Pt/C J.M.

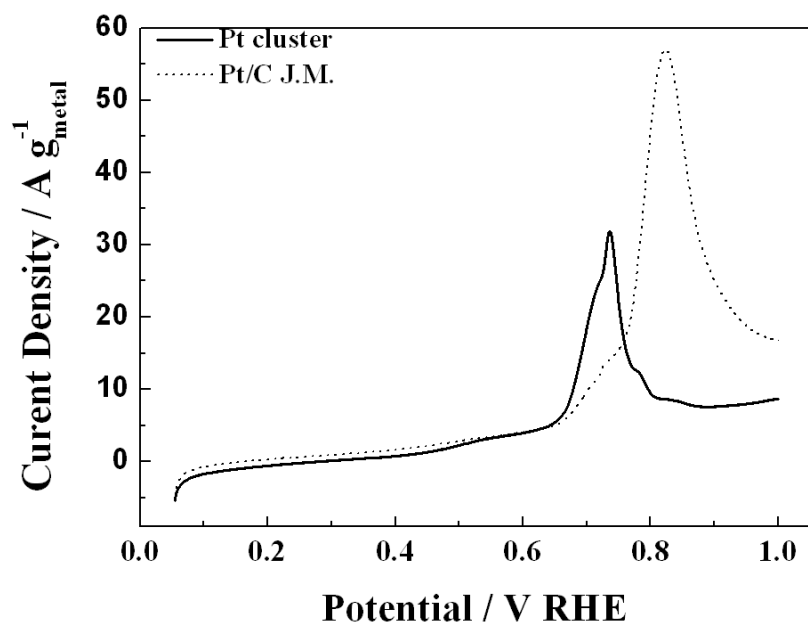


Fig. 3.6 CO_{chem} oxidative stripping voltammograms of Pt cluster and Pt/C J.M.

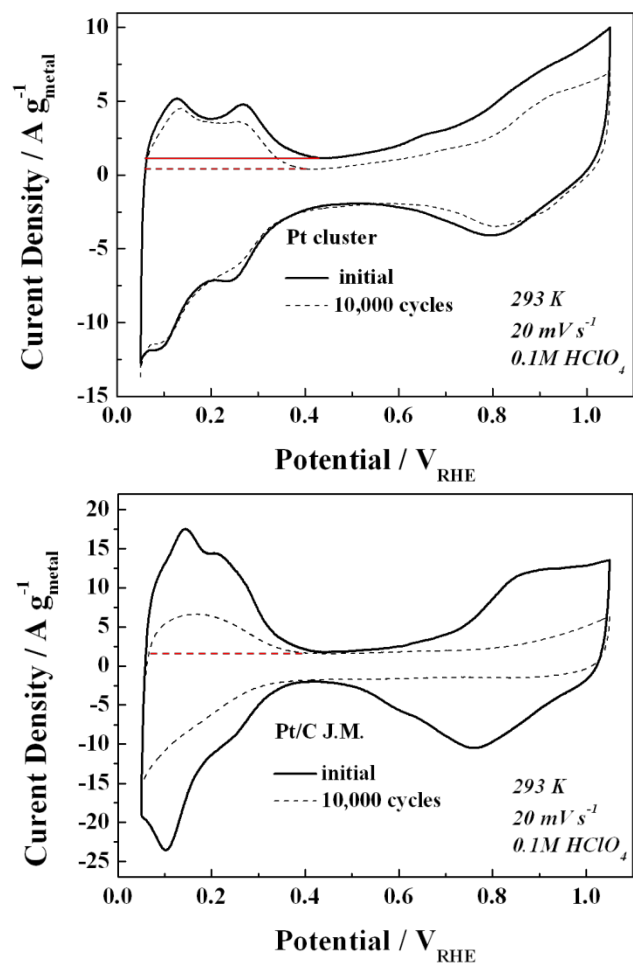


Fig. 3.7 Cyclic voltammogram of Pt cluster and Pt/C J.M. after ADT test.

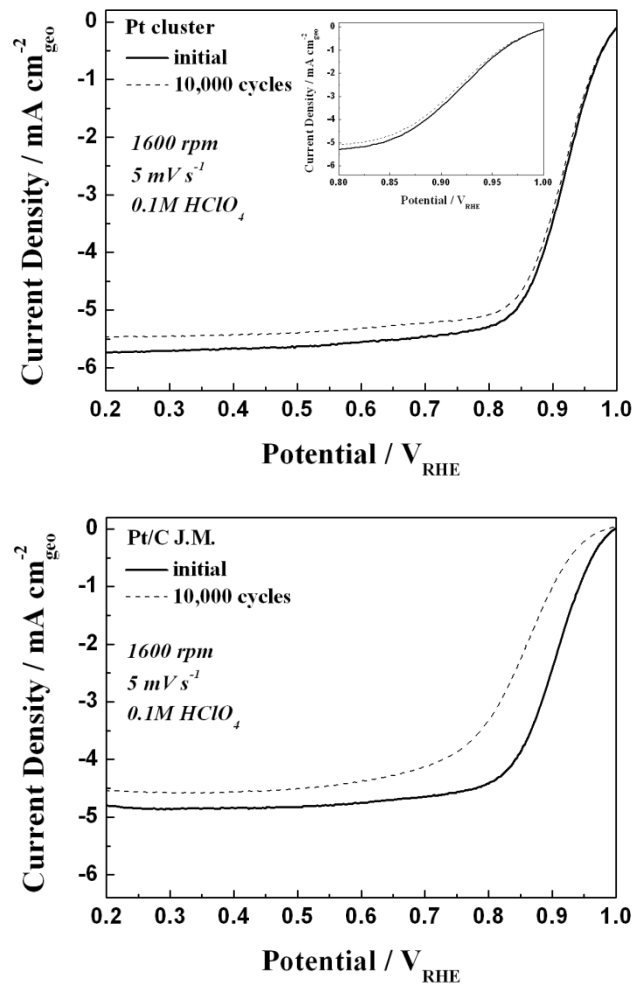


Fig. 3.8 ORR polarization curve of Pt cluster and Pt/C J.M. after ADT

3.2 Urchin like PtNi nanostructure

3.2.1 Urchin like PtNi nanostructure

The Proton exchange membrane fuel cells (PEMFCs) are the most promising renewable energy technologies to solve the exhaustion of fossil fuel and oil because of the advantages such as low operating temperature, high power density, low production of byproducts leading to the pollution and climate change induced by fossil fuel combustion [14]. Until now, platinum group metal (PGM)-based materials are a dominant class of electrocatalyst for efficient electrochemical energy conversion devices. However, commercialization of PEMFC's has been hindered due to the slow kinetics of the oxygen reduction reaction (ORR), which, in turn, decreases the overall performance of PEMFCs [15]. In addition, the scarcity and high cost of Pt metal drives up the cost of manufacturing, fuel cells. Therefore, a majority of fuel cell research focuses on finding catalysts that not only reduce the amount of Pt used but also enhances the catalytic activity and stability of the ORR. In order to address these requirements, several approaches have been developed, such as making nanostructures to increase the surface-to-volume ratio [15] controlling the shapes to increase the number of active sites on Pt nanoparticles [16] and alloying two or more non-precious metals into the nanostructures [17].

Markovic and co-workers demonstrated that Pt-Ni bimetallic material is one of the most promising candidates showing enhanced performance for the ORR [23]. Recently,

Yang group reported the synthesis of truncated octahedral Pt₃Ni nanoparticles and showed enhanced electrochemical performance compared to commercial Pt catalyst [27]. Fang and co-workers synthesized Pt₃Ni nanooctahedra and nanocube nanoparticles to compare activity of {111}- and {100}-bounded nanocatalysts [28]. Carpenter and co-workers developed the synthesis of Pt-Ni bimetallic nanoparticles without capping agents [29]. Although there are a few papers considering the synthesis of Pt-Ni bimetallic nanoparticles, their morphology control has been not intensively investigated until now. We herein report on the simple synthesis of urchin like Pt-Ni nanostructures through one-pot synthesis from thermolysis of metal acetylacetonate mixture solution. In order, to achieve control of the composition of our synthesized Pt-Ni nanostructures, the molar ratios of the precursors were adjusted. We demonstrated that these synthesized nanostructures exhibited better electrocatalytic performance compared to commercial Pt and Pt₃Ni catalyst. We performed several kinds of control experiments to optimize the synthesis conditions and understand the formation mechanism. When only Pt(acac)₂ was used as the precursor, truncated Pt nanoparticles with size of 30 nm were formed. On the other hand, when only Ni(acac)₂ was used, no particles were produced, which showed that it is hardly difficult to decompose Ni(acac)₂ at that temperature. This result showed that Ni(acac)₂ is required in the synthesis to control morphology and generate urchin like nanostructures. Optimal synthesis conditions were found by varying heating rates, temperature, and concentration of surfactants. It was found that multi-pod shaped Pt-Ni nanostructures were observed when the synthesis was conducted under other heating rates.

The use of only one capping agent produced aggregates consisting of spherical nanoparticles.

To understand the formation mechanism, we took aliquot samples and analyzed them with TEM and ICP at various stages during the synthesis. No particles were obtained until temperature reached to 220 °C, which indicated no reaction in the mixture solution occurred.

At 220 °C the color of mixture solution started to change, showing nucleation occurred. When an aliquot of the mixture solution at this temperature was taken and analyzed by ICP, we obtained the result that no Ni element was detected and Pt element was observed, showing that only Pt nanostructures were generated at 220 °C. As the reaction temperature increased, Ni concentration in the nanostructures increased, indicating that the Ni metal was reduced and incorporated into the Pt nanoparticles. The final products were Pt₃Ni bimetallic nanostructures with an urchin like morphology (Fig. 3.9). Recently, Li demonstrated the synthesis of Au-Co core-shell nanocrystals and Au-Ni spindly nanostructures using a noble-metal-induced reduction (NMIR) process [45]. In this system, the coexistence of octadecylamine (ODA) and Au metal resulted in the reduction of Co²⁺ and Ni²⁺ and Au-Co core-shell nanocrystals and Au-Ni spindly nanostructures were successfully synthesized although it is hardly difficult to reduce Co²⁺ and Ni²⁺ by ODA or noble metals. In addition, he indicates that bimetallic nanocrystals can be successfully obtained by controlling the experimental conditions using NMIR strategy. Therefore, the formation of Pt-Ni nanostructures in our synthetic system can be explained

by NMIR process. HDA and 1-ACA don't reduce Ni ions, but the addition of Pt metal makes the reduction of Ni ions viable. Fig. 3.10 shows a schematic diagram of the synthesis of Pt-Ni bimetallic nanostructures by NMIR process.

3.2.2 Crystalline and surface structure of urchin like PtNi

To reveal distribution of Pt and Ni metal in the products, energy dispersive spectroscopy (EDS) mapping analysis was performed. Fig. 3.9 shows that Pt and Ni element were evenly distributed in nanostructure, indicating formation of Pt-Ni alloy nanostructures. When the crystal structure was verified, all peaks of the X-ray diffraction (XRD) pattern can be assigned to the (111), (200), (220), and (311) lattice planes of a face-centered cubic (fcc) Pt-Ni bimetallic nanostructure [26-27]. When the intensity ratios between main two peaks ($I_{(200)}/I_{(111)}$) was calculated, the values obtained were 0.39 for PtNi, 0.36 for Pt₂Ni, and 0.38 for Pt₃Ni nanostructures. The fact that all 3 values are below the values of the bulk materials (0.53) indicates the (111) diffraction was dominant [29]. As the Ni composition in the Pt-Ni bimetallic nanostructures is rich, the (111) peak slightly shifts to higher degree from reference peak position of Pt, showing a decrease of lattice constant due to the replacement of Pt with Ni in the crystal lattice.

3.2.3 Electrochemical characterization of urchin like PtNi

To evaluate electrochemical activity of urchin like Pt-Ni bimetallic nanostructures, nanostructures were loaded on to carbon (Vulcan XC-72) via a hexane solution. Polarization curves and cyclic voltammetry (CV) for urchin like Pt-Ni nanostructures with three different compositions and commercial Pt catalyst as reference are displayed in Fig. 3.13. It revealed that Pt₃Ni nanostructures exhibit the best ORR activity among them and Pt-Ni nanostructures have lower activity than commercial Pt catalyst, indicating that the ORR

It is well known that the activity of Pt-Ni nanostructures is dependent on its composition. The result has good agreement with the observation from the previous works of Pt-Ni bimetallic nanocatalyst [32].

We used cyclic voltammetry to investigate the difference of electrochemical properties between urchin like Pt₃Ni nanostructures and commercial Pt₃Ni E-tek. CV was recorded at 20 °C in an Ar purged 0.1 M HClO₄ at with the scan rate of 20 mV s⁻¹. Fig. 3.13 shows CV curves of urchin like Pt₃Ni and Pt₃Ni E-tek. Intriguingly, the oxide formation/reduction potential of urchin like Pt₃Ni is more positive than that of Pt₃Ni E-tek, which the adsorption may be attributed to a growth of 1D structure.[13] Specific activity and mass activity of urchin like Pt₃Ni nanostructures was 2.4 times and 2.4 times of that of that of Pt₃Ni E-tek (Fig. 3.14).

It is known that (111) plane exhibits better activity than (100) plane in Pt-Ni bimetallic compounds [25-27]. The enhanced ORR activity of urchin like Pt₃Ni nanostructures is caused by the substantial amount of higher electrochemical active (111) plane on the surface in nanostructures. Fig. 3.9 (b) indicated that arm in nanostructures consisted of (111) planes rather than (100) planes. Fig. 3.12 XRD profile also manifests the unique characteristic of urchin like Pt₃Ni nanostructures, which the increased sharpness of the (111) peak has a good correspondence with the increment of (111) facets. Results of cyclic voltammetry and ORR polarization curves after 4000 cycles of ADT results are manifested on Fig. 3.15 and 3.16. The initial ESA of urchin like Pt₃Ni (5.047 m² g⁻¹) was decreased to 2.933 m² g⁻¹. For Pt₃Ni E-tek the ESA was decreased from 32.614 m² g⁻¹ to 14.423 m² g⁻¹. The ORR activity showed a correlation with the ESA result. The half-wave potential of urchin like Pt₃Ni shifted from 0.92 V to 0.793 V. In case of Pt₃Ni E-tek the half-wave potential shifted from 0.90 V to 0.69 V. The role of urchin like structure was verified by XANES analysis to support the enhancement of urchin like Pt₃Ni in comparison with Pt₃Ni E-tek. Fig. 3.17 represents the Pt L_{III} edge and Ni K edge of urchin like Pt₃Ni and Pt₃Ni E-tek. From white line analysis, it can be explained which sample has a favorable electronic structure for ORR. The intensity of Pt L_{III} edge decreased and Ni K edge increased for urchin like Pt₃Ni. In other words, it means that urchin like structure is favorable transferring Ni electron to Pt and fill the d-band down shifts the d-band center.

In conclusion, we demonstrated the facile synthesis of urchin like Pt-Ni nanostructures

by controlled one-pot NMIR process. The composition control of Pt-Ni nanostructures was achieved by varying molar ratio of $\text{Pt}(\text{acac})_2$ and $\text{Ni}(\text{acac})_2$. Cyclic voltammetry method was used to investigate the difference of electrochemical properties between urchin like Pt_3Ni nanostructures and commercial Pt_3Ni E-tek. Intriguingly, the oxide formation/reduction potential of urchin like Pt_3Ni is more positive than that of Pt_3Ni E-tek, which the adsorption may be attributed to a growth of 1D structure. The urchin like Pt_3Ni nanostructures showed 2.4 times higher electrochemical oxygen reduction activity than the commercial Pt_3Ni E-tek for ORR.

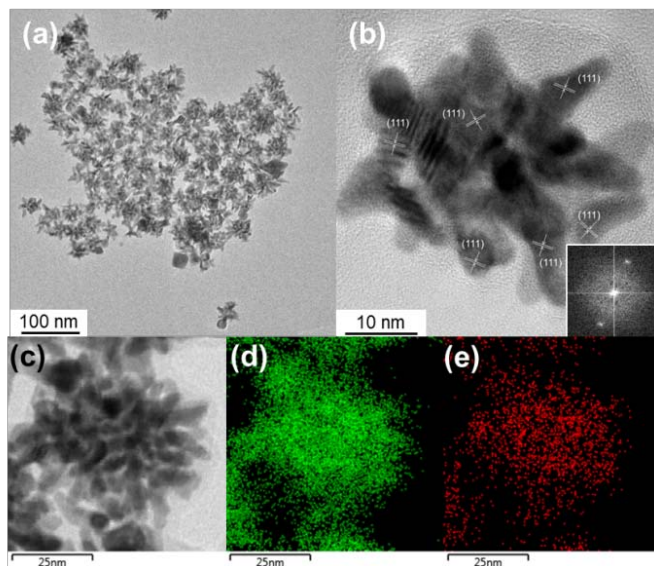


Fig. 3.9 TEM and EDX of urchin like Pt_3Ni nanostructure

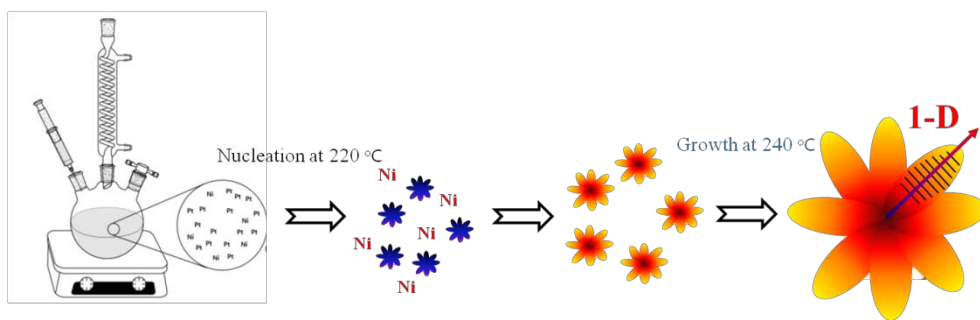


Fig. 3.10 Scheme of synthesis of urchin like Pt_xNi with one dimension.

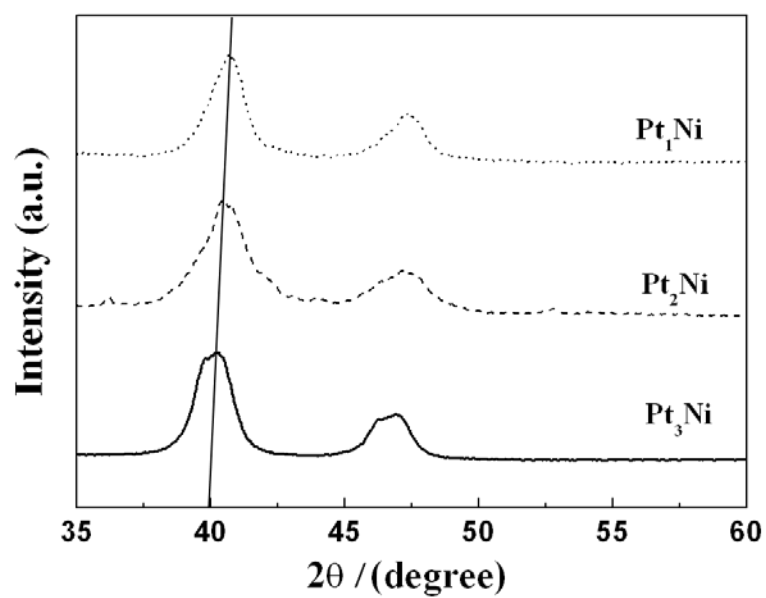


Fig. 3.11 X-ray diffraction pattern of Pt₃Ni, Pt₂Ni, and Pt₁Ni.

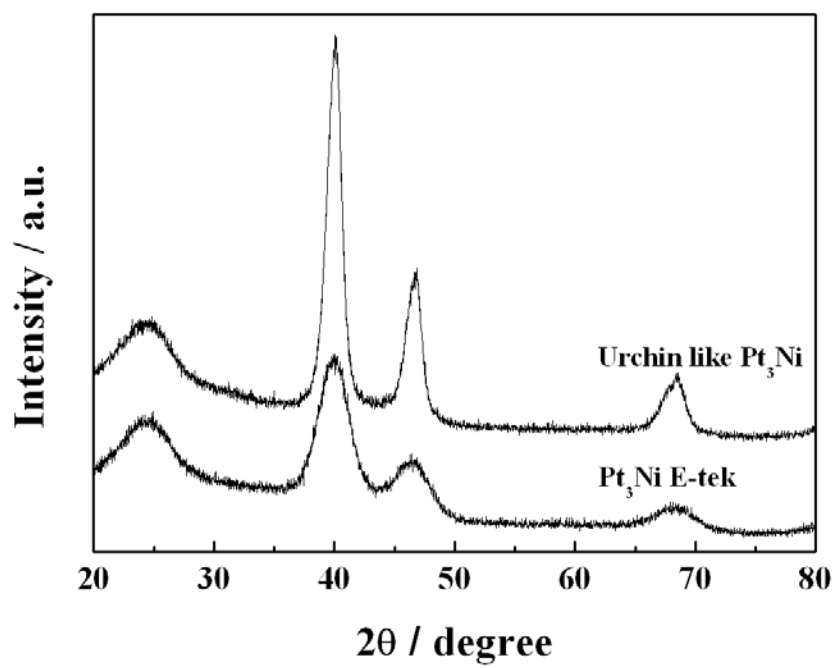


Fig. 3.12 X-ray diffraction pattern of Pt₃Ni and Pt₃Ni E-tek.

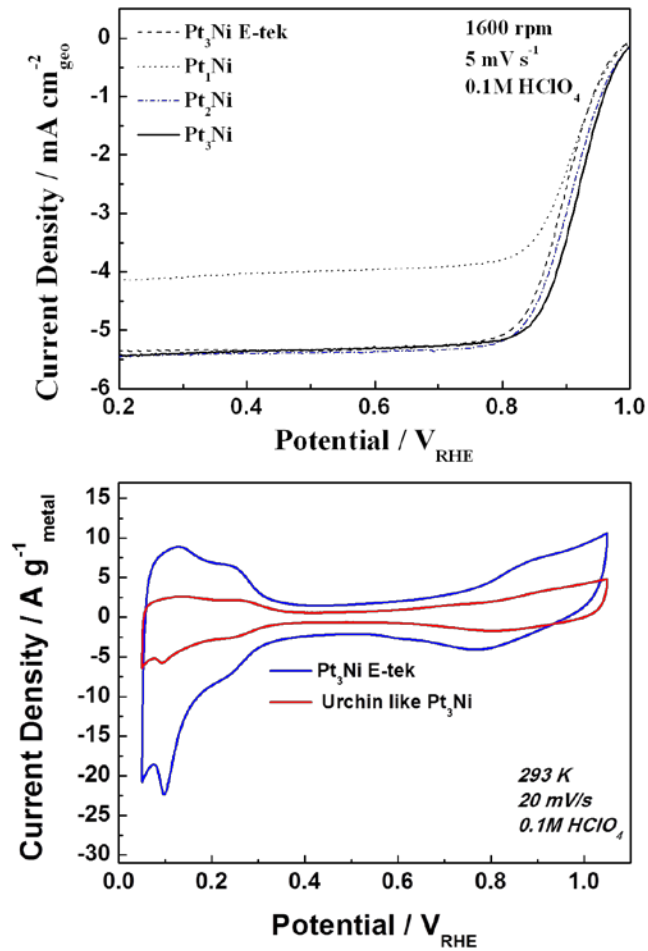


Fig. 3.13 Oxygen polarization curves of Pt_xNi and cyclic voltammety of urchin like Pt₃Ni and Pt₃Ni E-tek.

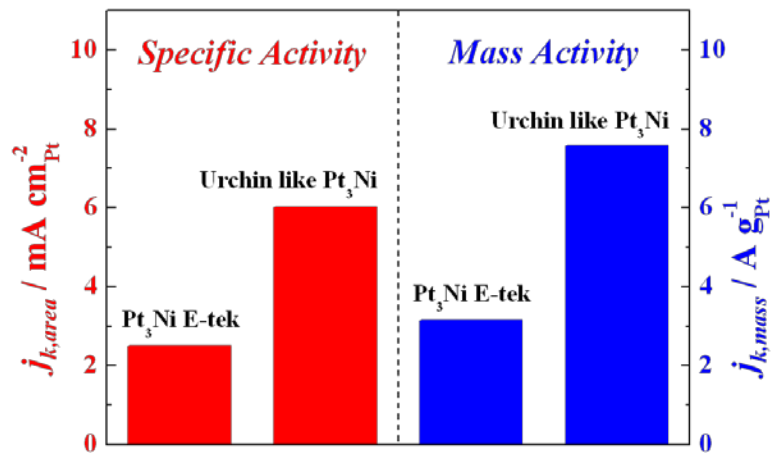


Fig. 3.14 Specific and mass activity of Pt₃Ni and Pt₃Ni E-tek.

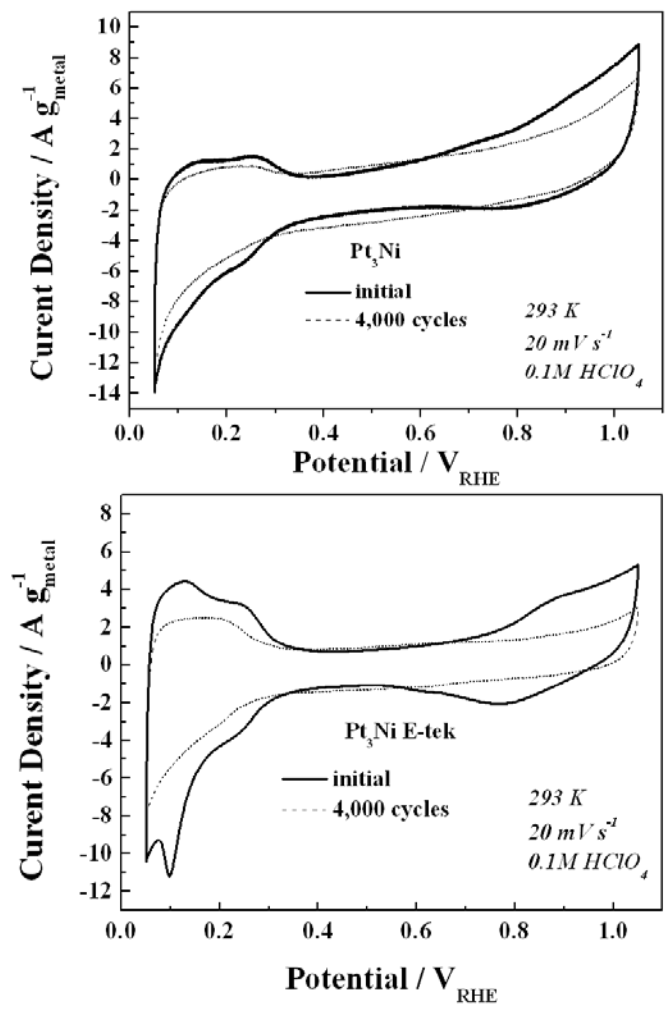


Fig. 3.15 Cyclic voltammetry of Pt₃Ni and Pt₃Ni E-tek after 4000 cycles ADT test.

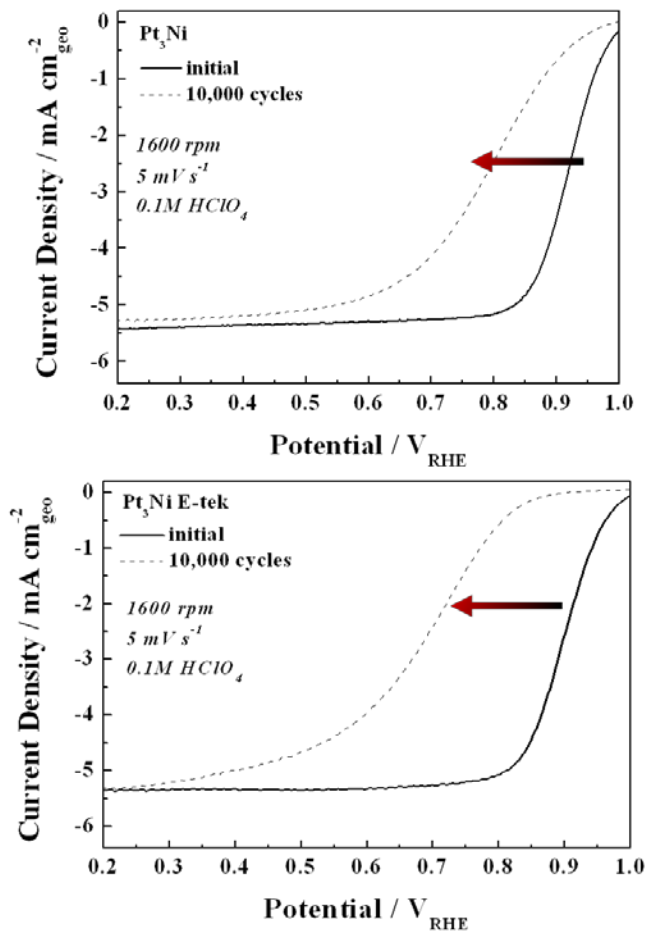


Fig. 3.16 Oxygen polarization curves of Pt₃Ni and Pt₃Ni E-tek after 4000 cycles ADT test.

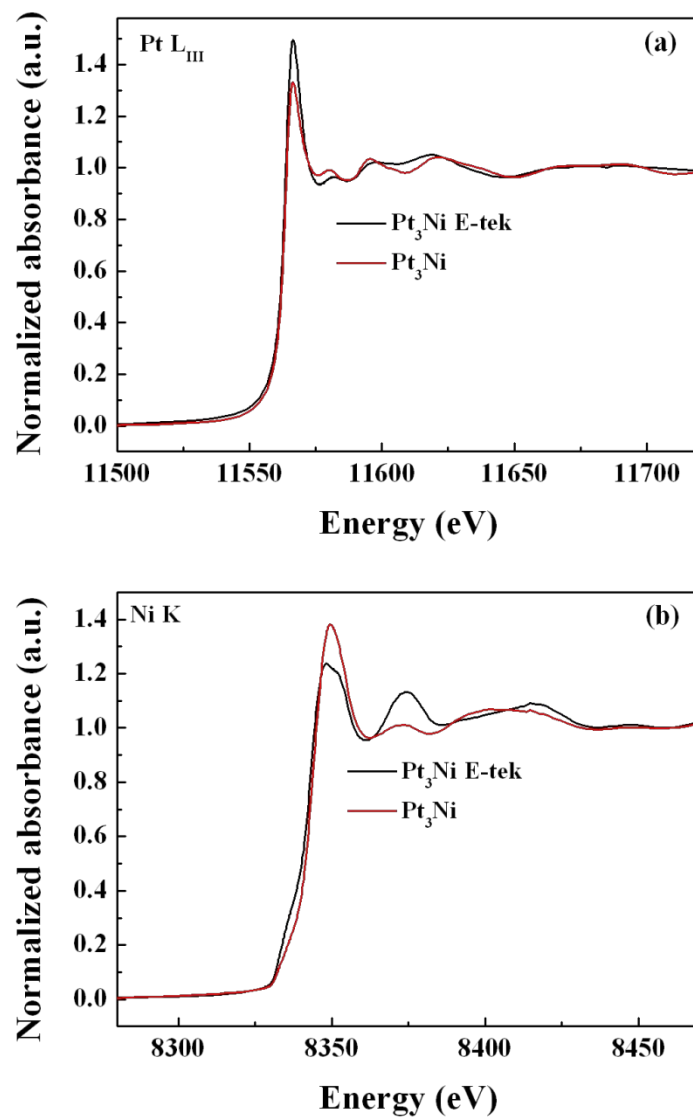


Fig. 3.17 XANES spectra of (a) Pt L_{III} edge and (b) Ni K edge for urchin like Pt₃Ni and Pt₃Ni E-tek.

3.3 Carbon supported PdFe nanoparticles

3.3.1 PdFe nanocatalyst

Polymer electrolyte membrane fuel cells (PEMFCs) are state of the art energy conversion devices for automotive and stationary applications, due to its high efficiency. However, the possibility of commercialization of PEMFCs is significantly obstructed by the high price of Pt and sluggish kinetic reaction of Pt with oxygen. A considerable amount of study has been done to decrease the usage of Pt while maintaining high oxygen reduction reaction (ORR) activity and low cost; forming Pt based alloy with other transition metals and core-shell structured nanoparticles [46-62]. However, these nanoparticles still holds the problem of using Pt. In consequence, ongoing research has been concentrated on forming non-Pt electrocatalysts which is primarily intended for lowering the cost of the PEMFC while possessing high ORR activity. Recently, many researchers focused their study on alloying Pd with cheap transition metals (M = Co, Fe, and Ni) for a substitution of Pt due to their modified valance band structure and lattice parameter. Adzic reported that if Pd₃Fe is heat treated in high temperature Pd layer is segregated and forms a same surface structure with Pd but possessing different electronic properties [46]. Shao et al. reported alloying Pd with Fe gives a higher ORR activity than with Co because a Fe atom size is smaller than a Co atom size [47]. The relationship between Pd-Pd bond distance and surface-specific activity was studied to gain information about the role of surface structure. Abruna et al. managed to obtain PdCo

nanocatalysts that have the structure of Pd rich on the surface and PdCo inside the core to enhance the ORR activity and to decorate Pt [48]. Tailoring the structure of PdCo by conducting a heat treatment at 500 °C in H₂ flow for 2 h yielded a core-shell structure and the enhancement of ORR activity.

Pd-Fe alloy nanoparticles show great performance for ORR in the PEMFC. However, most of them were single crystals which have certain disadvantages for the commercialization. In this study, we synthesized a well dispersed Pd-Fe alloy nanoparticles supported on a carbon so it can be commercialized due to mass production and shed a light on the post heat treatment to enhance the ORR activity of the PdFe nanocatalyst.

3.3.2 Crystalline structure of PdFe after heat treatment

PdFe alloy nanoparticles with different composition XRD result is manifested in Fig. 3.18. (220) XRD peak of pristine Pd₃Fe₁, Pd₁Fe₁, Pd₁Fe₃ allows to calculate the particle sizes of the pristine PdFe samples using Scherrer's equation;

$$L = \frac{K\lambda}{B \cos \theta}$$

The particle sizes were 3.1 nm, 2.9 nm, 2.7 nm for Pd₃Fe₁, Pd₁Fe₁, and Pd₁Fe₃, respectively. Additionally, the lattice parameters of each samples are denoted in table 3.1.

Jeon reported Pd nanoparticles synthesized with $\text{Pd}(\text{acac})_2$ have the trace of carbon attributed to long capturing ligands from the acetylacetonate [63].

In order to remove this carbon residue high temperature annealing in air flow process was applied. However, Fe has an intrinsic property of quickly turning into an oxide material. To prevent this affect PdFe nanocatalysts requires heat treatment in H_2 flow under high temperature. Yang et al. modified the surface compositions and morphologies of $\text{Pd}_3\text{Fe}(111)$ alloy single crystal by high temperature heating in UHV. As a result, heat treated $\text{Pd}_3\text{Fe}(111)$ showed five to eight times more active than $\text{Pd}(111)$ and twice as active as $\text{Pt}(111)$. The lower surface energy of Pd induces surface segregation to the topmost surface layer of Pd-Fe alloy. This high heat treatment will also provoke Pd rich PdFe core structure (Fig. 3.19). In addition, due to the high temperature post heat treatment, partially reduced Fe nanoparticles can transform into fully reduced Fe nanoparticles which leads to higher alloy with Pd nanoparticles. Therefore, we proceeded an annealing process up to 300 °C and 500 °C in H_2 atmosphere after the 200 °C post heat treatment in air. All the post heat treated PdFe alloy nanoparticles peak shifted to higher angle compared to the pristine samples which is in good agreement with the result that Jeon reported (Fig. 3.21) [63]. This phenomenon can be explained from two reasons. First, the carbon dissolution which provokes a volume change. When the volume of the sample shrinks the lattice parameter value shows the same propensity. Due to lower lattice parameter the XRD peak shifts to higher angle. Second, the alloying degree between Pd and Fe has been increased. TEM images of the PdFe before and after the post heat

treatment are manifested in Fig. 3.20. Fig. 20 (a), (d), and (g) there were no significant difference of the morphology and size of the PdFe nanocatalysts. However, in Fig. 3.20 (b)(c), (e)(f), and (h)(i) drastic change of size and morphology were detected from the 300 °C and 500 °C post heat treatment. The average particle sizes of 500 °C heat treated Pd₃Fe₁, Pd₁Fe₁, and Pd₁Fe₃ calculated from XRD were 4.10 nm, 3.72 nm, 3.70 nm, respectively.

3.3.3 Electrochemical characterization of PdFe after heat treatment

The cyclic voltammetry data of pristine PdFe alloys and 500 °C post heat treated PdFe nanocatalysts manifest the distribution charge under the H_{upd} potential region (Fig. 3.24). The H_{upd} region gives us an information of surface composition. By and large, Pd is a well known metal for strong absorption of H₂. Therefore, if Pd metal is rich outside the surface hydrogen absorption peak near 0.2 V arises. In Fig. 3.24 (a) it is obvious that pristine PdFe samples obey the propensity explained above. On the other hand, for 500 °C post heat treated PdFe samples Pd₁Fe₁ show the highest hydrogen absorption peak around 0.2 V which implies that when PdFe samples are heat treated Pd₁Fe₁ has the most Pd at outer surface.

The rotating disk electrode (RDE) technique was used to conduct assessment of oxygen reduction reaction in 0.1 M HClO₄ solution. The ORR polarization curve measurements were initiated in the positive direction from 0.05 V vs RHE. In Fig. 3.25 (a), it is

manifested that half-wave potentials increased in following order: $\text{Pd}_1\text{Fe}_3 < \text{Pd}_1\text{Fe}_1 < \text{Pd}_3\text{Fe}_1$ with the half wave value of 0.71 V, 0.75 V and 0.78 V, respectively. However, the ORR activity of PdFe samples were insufficient in comparison with commercial Pt. In contrast, 500 °C post heat treated PdFe samples exhibited dramatic increase in ORR half wave potential. As shown in Fig. 3.25 (b) the half-wave potentials increased in following order: $\text{Pd}_3\text{Fe}_1 < \text{Pd}_1\text{Fe}_3 < \text{Pd}_1\text{Fe}_1$ (0.77 V < 0.89 V < 0.92 V). Through the electrochemical characterization of PdFe and post heat treated PdFe samples using cyclic voltammetry and ORR measurement we found a correlation with Pd rich surface and enhancement of ORR activity. Pd rich surface gives a rise to an enhancement of ORR activity,

3.3.4 XANES characterization of PdFe after heat treatment

The transition of oxidation state of Pd and Fe were verified by XANES analysis in order to clarify the peak shifts of XRD. Pd K edge can be utilized for assessing the qualitative changes in the oxidation state of the Pd_3Fe_1 , Pd_1Fe_1 , and Pd_1Fe_3 . Fig. 3.22 represents the alternation of Pd K edge of the PdFe samples in accordance with the temperature. All the samples' Pd K edge white line intensities were analogous to one another even after the increase of the temperature in the post heat treatment. Which means that Pd was fully reduced as a metal before the post heat treatment was conducted. However, for Fe the K edge white line intensities exhibited different transition tendency compared with that of Pd. As shown in Fig. 3.23, the pristine Fe had the highest white line intensity on account of low reduction potential of Fe which aggravates the hindrance of reduction to metallic

phase. Consequently, this result states that partially reduced Fe oxide or hydroxide exist for the pristine PdFe samples. To enhance the amount of Fe metallic phase post heat treatment temperature was increased and as the temperature increased, Fe began to be reduced and eventually formed the metallic phase. The increment of Fe metallic phase induces the decrement of white line intensity which is in inversive relationship.

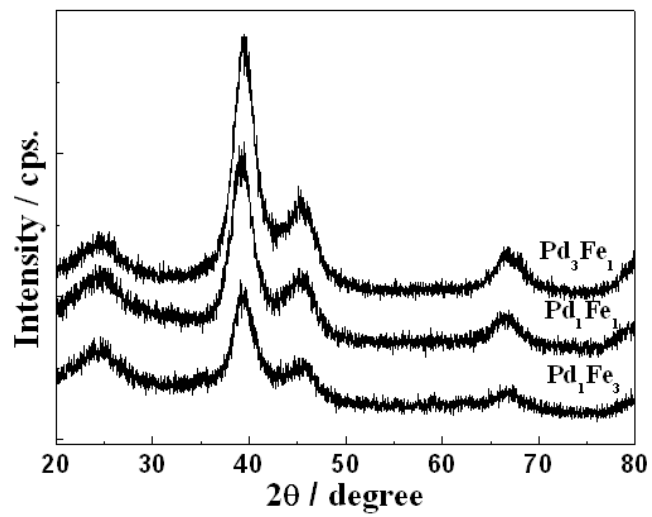


Fig. 3.18 XRD profiles of pristine PdFe samples.

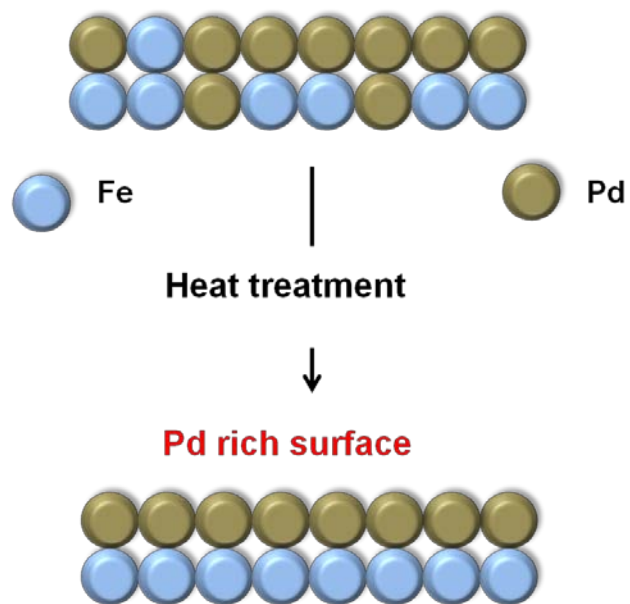


Fig. 3.19 Scheme of obtaining Pd rich surface by heat treatment.

Sample	Peak positions(220)	Lattice Parameter	Particle size
Pd ₃ Fe ₁	66.905	3.9556	3.009
Pd ₁ Fe ₁	66.448	3.9796	3.245
Pd ₁ Fe ₃	66.620	3.9705	3.772

Table 3.1 Lattice parameter values for PdFe samples.

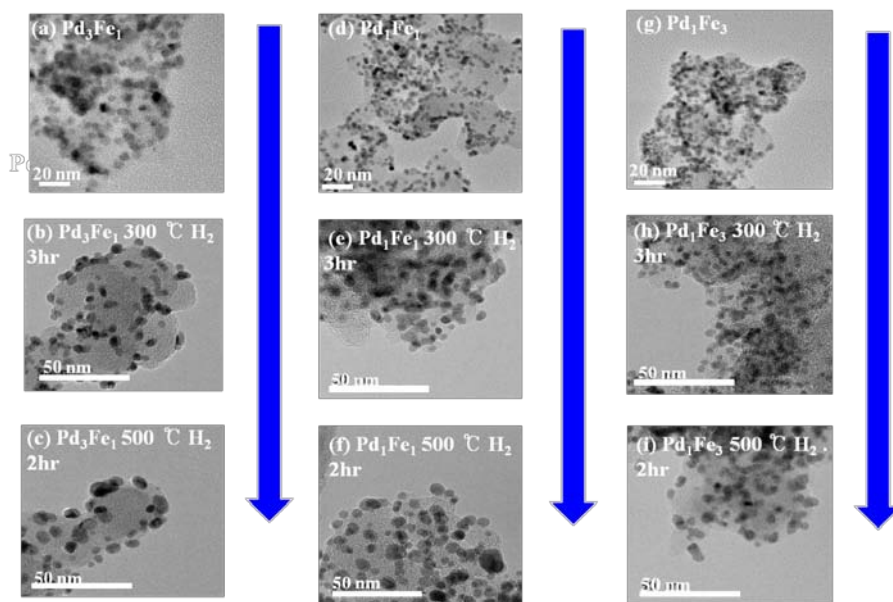


Fig. 3.20 TEM images of pristine, 300 °C, and 500 °C post heat treated PdFe samples (a)(b)(c) Pd₃Fe₁, (d)(e)(f) Pd₁Fe₁, (g)(h)(i) Pd₁Fe₃.

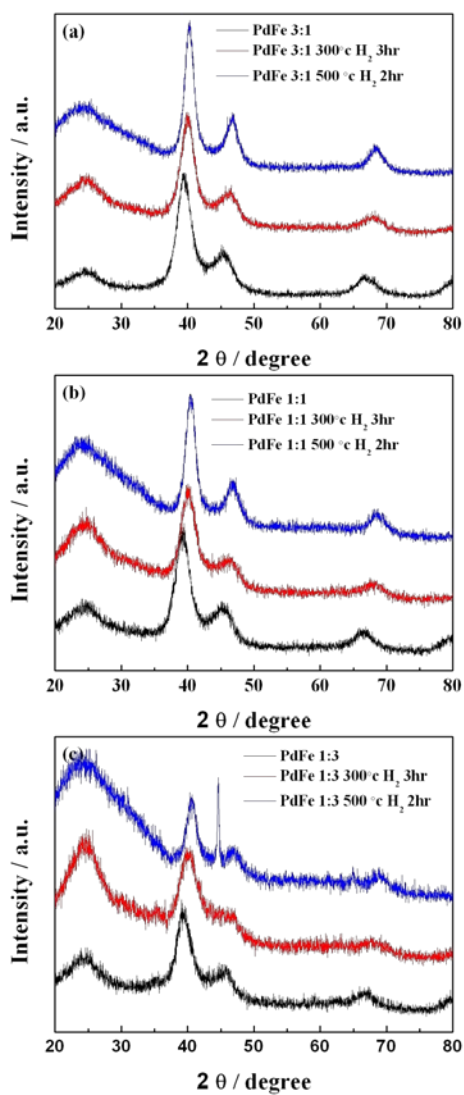


Fig. 3.21 XRD profiles of pristine, 300 °C, and 500 °C post heat treated PdFe samples.

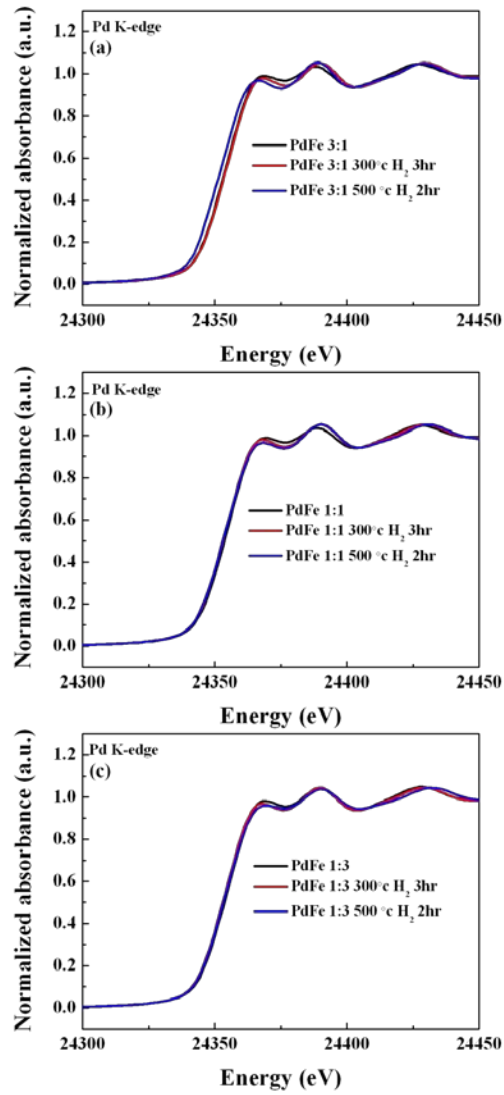


Fig. 3.22 XANES spectra of Pd K edge pristine, 300 °C, and 500 °C post heat treated PdFe samples.

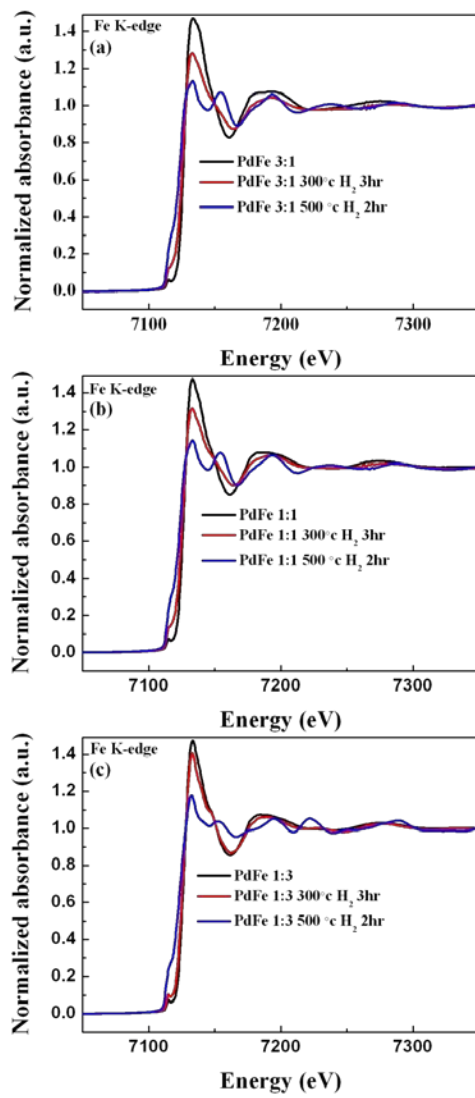


Fig. 3.23 XANES spectra of Fe K edge pristine, 300 °C, and 500 °C post heat treated PdFe samples.

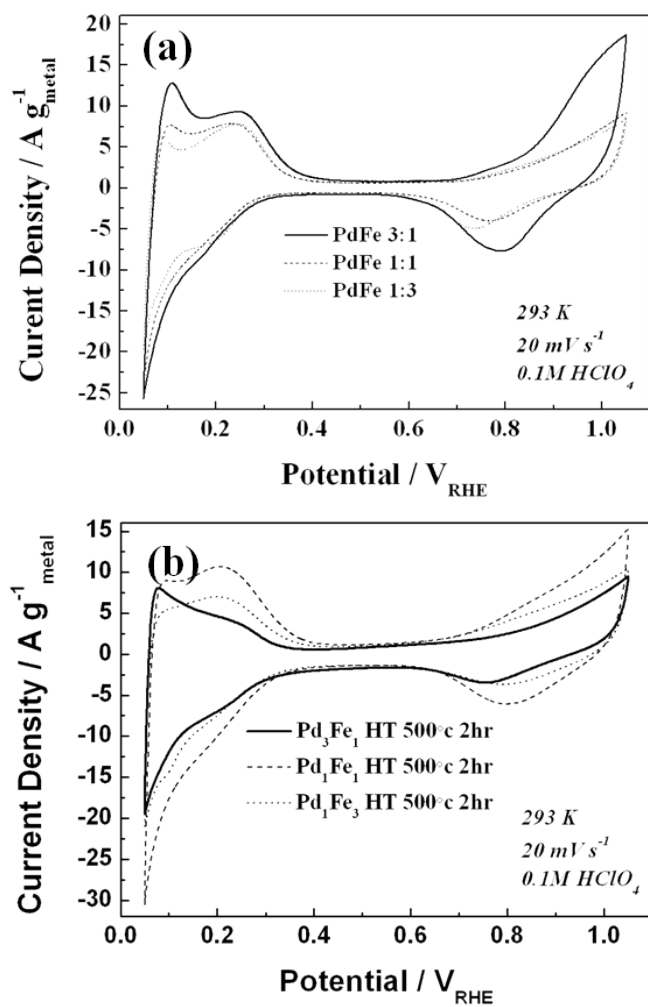


Fig. 3.24 Cyclic voltammetry of pristine PdFe and 500 °C post heat treated PdFe samples.

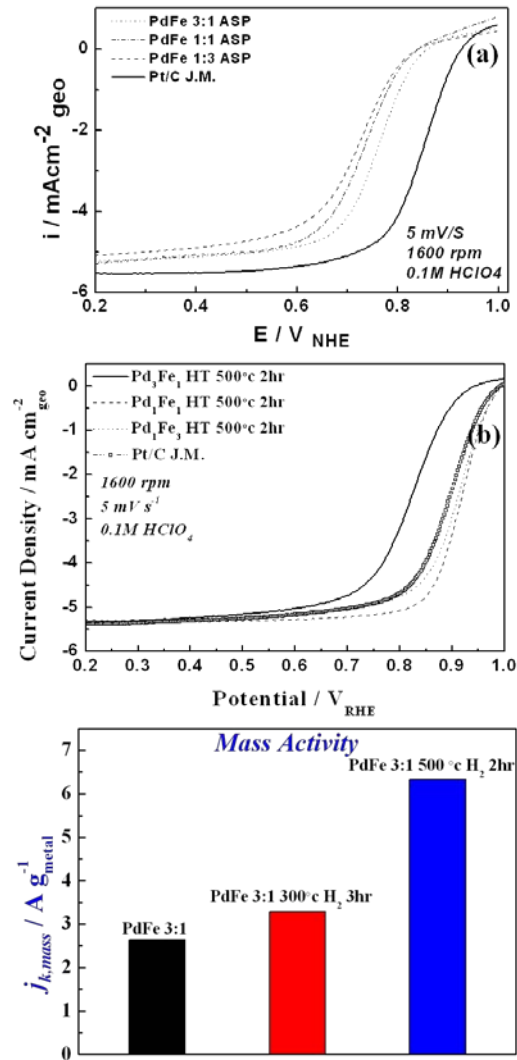


Fig. 3.25 Oxygen polarization curves and mass activity of pristine, 300 °C, and 500 °C post heat treated PdFe samples.

3.4 Pt decorated on PdFe core nanoparticles

3.4.1 Carbon supported PdFe@Pt nanoparticles

For many years, designing new catalysts for the use in low temperature fuel cells have been a major area of research. Possible catalysts have been demonstrated with the help of theoretical studies. From these simulations, researchers have begun to research different composition ratios of noble metal and transition metal alloys, some of which have catalytic ORR activity comparable to a Pt catalyst. However, in contrast to high ORR activity the alloyed catalysts possess severe low stability which is a huge obstacle for the commercialization. To overcome this problem core-shell structured catalyst received a lot of attention from the researchers recent years. Core-shell structured catalyst is considered as a prominent catalyst which can reconcile durability and Pt utilization. Adzic et al. reported Pd core protected by Pt monolayer shell exhibited high stability compared with Pt catalyst. In addition, the theoretical calculations using density functional theory with the concept of oxygen adsorption energy and vacancy formation energy have been applied. The computational screening was performed on the overlayer-substrate system in order to diminish the effect of complexity originated from multiple atoms in the nanoparticles (Fig. 3.26). As a result, it is shown that Pd₃Fe@Pt catalyst is the most suitable catalyst for high stability. Therefore, we studied the surface composition

of PdFe core-Pt shell nanoparticles by using XRD and electrochemical measurements. PdFe 3:1 nanoparticles post heat treated at 300 °C were chosen as a core due to its similarity in dispersion and particle size in comparison with the pristine PdFe 3:1 nanoparticles with high ORR activity.

3.4.2 Crystalline and surface structure of Carbon supported

PdFe@Pt nanoparticles

As the atomic ratio of Pt/PdFe increases the XRD peak was shifted to a lower angle closer to Pt (111) peak and had the inclination to increase in size (Fig. 3.27). Through the XRD analysis it was possible measuring the changes of the particle size of the PdFe@Pt. The particle size for PdFe, Pt[0.1]/PdFe, Pt[0.5]/PdFe, and Pt[1]/PdFe was 2.71 nm, 2.89 nm, 3.18 nm, and 3.24 nm, respectively (Table 3.2).

3.4.3 Electrochemical characterization of Carbon supported

PdFe@Pt nanoparticles

Electrochemical measurements were performed in a room temperature (20 °C) controlled electrolyte with a conventional three electrode electrochemical cell comprised of a glassy carbon working electrode, a platinum wire counter electrode, and a saturated calomel reference electrode (SCE). The reference electrode potential was corrected to a reversible hydrogen electrode (RHE). Catalyst ink was prepared with 5 wt % Nafion solution, 2-propanol, and 0.01 g of Pt cluster catalyst. The catalyst ink (3 µl) was dropped onto the working electrode and dried at 60 °C oven for 15 min. Pre cycling of the catalyst

was taken in an Ar saturated 0.1 M HClO₄ electrolyte before cyclic voltammogram (CV) measurement. The potential range, scan rate, and cycling number of the pre cycling were 0 V to 0.4 V, 100 mV s⁻¹, and 30 cycles, respectively. After the pre cycling, when the double layer is stable and the surface cleaning is completed, cyclic voltammogram measurement was conducted with a scan rate of 20 mV s⁻¹ for 3 cycles. In order to survey the ORR activity of the PdFe@Pt nanoparticles the ORR measurement was conducted on the rotating disk electrode (RDE). ORR polarization curve was obtained in an O₂ saturated 0.1 M HClO₄ electrolyte at a scan rate of 5 mV s⁻¹ and at a rotating rate of 1600 rpm. For CO and CO₂ oxidation the adsorption of CO and CO₂ were conducted at 0.02 V and 0.01 V, respectively. Fig. 3.28 (a) shows cyclic voltammograms of carbon supported PdFe (20 wt %) and PdFe@Pt nanoparticles with different Pt/PdFe atomic ratios. The stepwise increase of Pt loading on PdFe nanoparticles shifts the reduction peak to a higher potential from 0.72 V to 0.8 V. This reduction peak potential shift manifests that Pt decorated PdFe surfaces are more stable from the surface oxidation than that of PdFe. However, the largest H_{upd} area was for Pt[0.5]/PdFe which also had the highest ORR activity in comparison with other Pt decorated PdFe nanoparticles.

As shown in Fig. 3.28 (b) the half wave potential ($E_{1/2}$) of Pt[0.1]/PdFe, Pt[0.5]/PdFe, and Pt[1]/PdFe are located at 0.857 V, 0.905 V, and 0.889 V, respectively. Pt[0.5]/PdFe exhibited the highest ORR activity compared to the other Pt decorated PdFe samples. PdFe core decorated with Pt structure exhibited enhancement in both the Pt utilization and ORR activity compared to Pt nanoparticles. Fig. 3.29 (a) shows CO oxidation cyclic

voltammograms of Pt decorated PdFe with different Pt/PdFe atomic ratios. As the amount of decorated Pt atoms escalates the CO oxidation peak shifts to lower potentials close to pure Pt. This phenomenon is believed to be caused by hydroxide formation of Pd at 1.1 V in acidic solution. In conclusion, the CO oxidation peak shift to low potential means that Pt atoms are gradually deposited on the PdFe core. However, CO gas has an intrinsic property that it can be adsorbed both on Pt and Pd. Therefore, in order to exclude the Pd effect the gas was changed to CO₂ because CO₂ does not adsorb on Pd atoms. From the Fig. 3.29 (b) it was clear that low amount of Pt atom decorated PdFe had a H_{upd} region in comparison with large amount of Pt atom decorated PdFe.

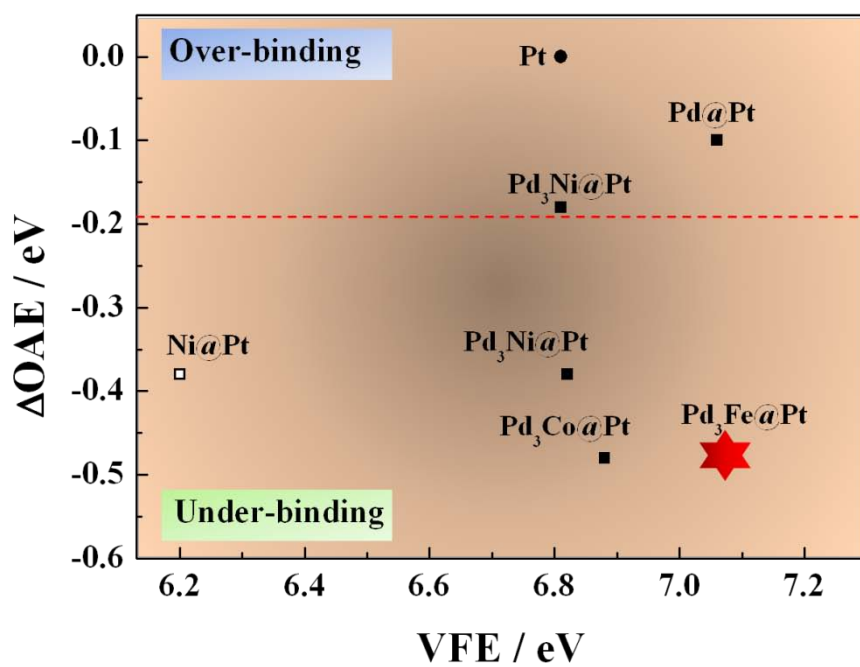


Fig. 3.26 Computational screening of Pt coated suitable core materials for the high activity and durability [64].

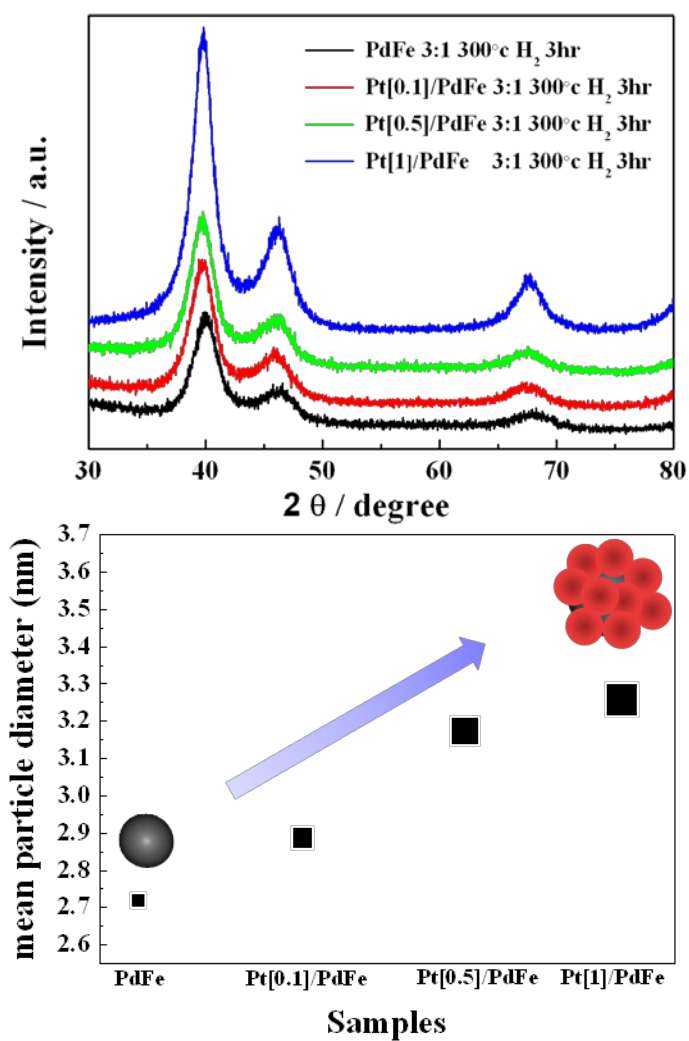


Fig. 3.27 XRD profiles of Pt decorated PdFe 3:1 300 °C H₂ 3hr.

Sample	Peak position (2 θ)	FWHM	Particle size (nm)
PdFe 3:1 300 °C H ₂ 3hr	67.96	2.7816	2.71
Pt [0.1]/PdFe	67.76	2.8241	2.89
Pt [0.5]/PdFe	67.65	3.3638	3.18
Pt [1]/PdFe	67.60	3.6970	3.24

Table 3.2 FWHM and particle size values for Pt decorated PdFe 3:1 300 °C H₂ 3hr.

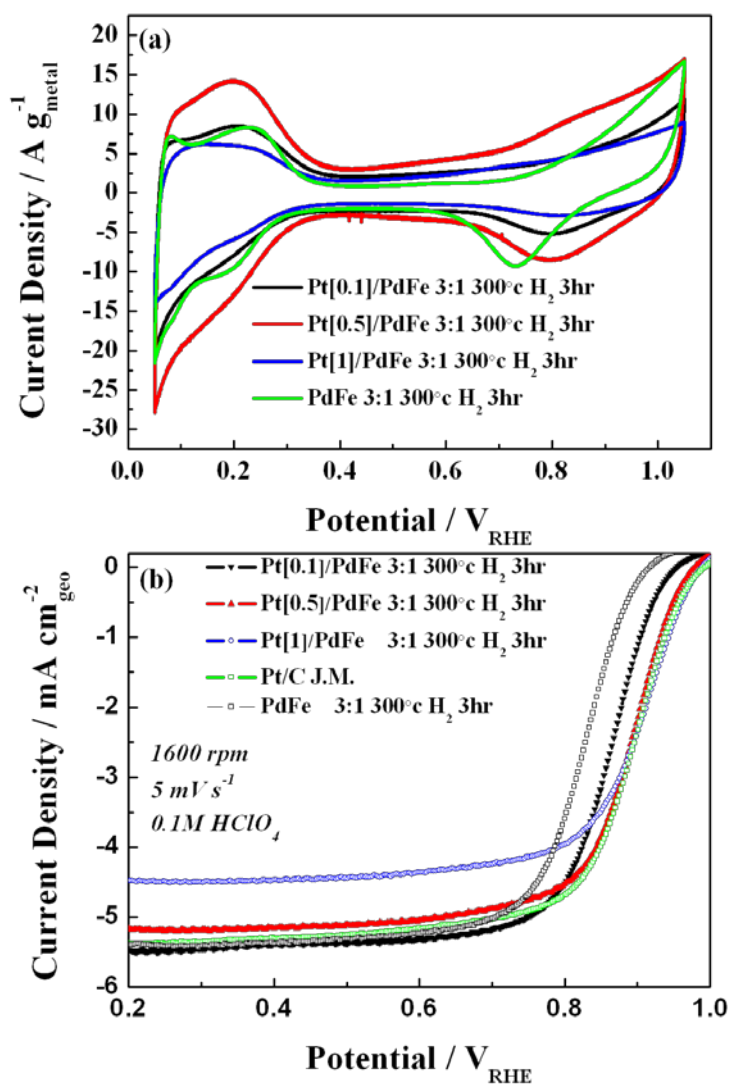


Fig. 3.28 Cyclic voltammograms and ORR polarization curves of Pt decorated PdFe 3:1 300 °C H₂ 3hr .

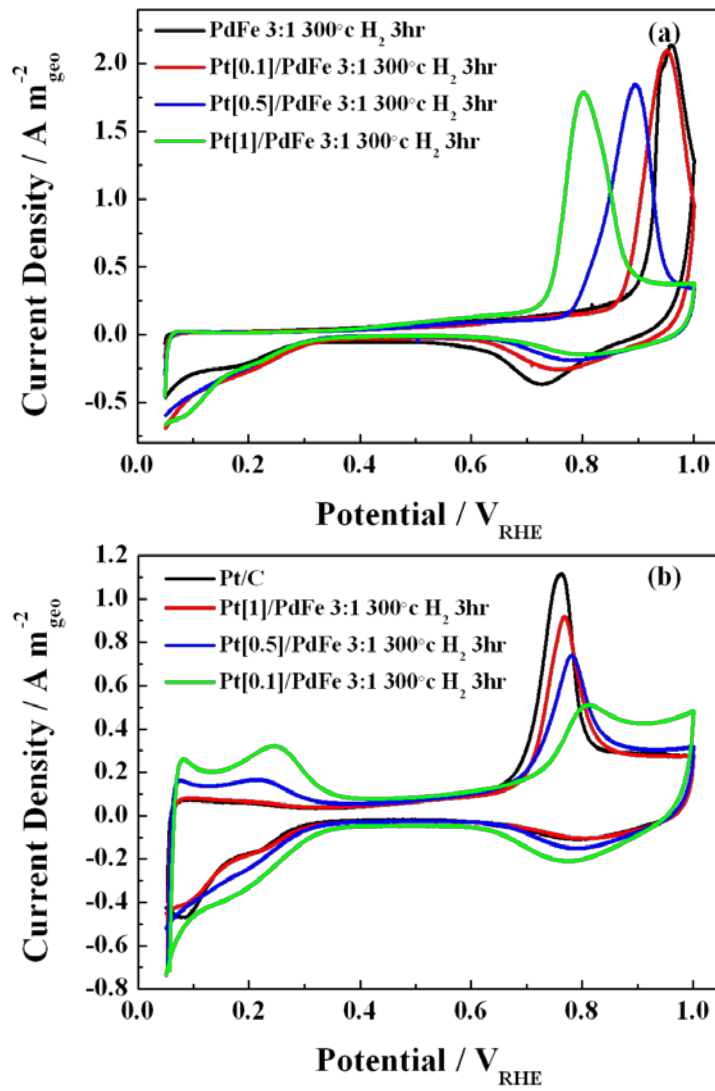


Fig. 3.29 CO and CO₂ oxidation curves of Pt decorated PdFe 3:1 300 °C H₂ 3hr.

3.5 References

1. D.-S. Kim, C. Kim, J.-K. Kim, J.-H. Kim, H.-H. Chun, H. Lee, Y.-T. Kim, "Enhanced electrocatalytic performance due to anomalous compressive strain and superior electron retention properties of highly porous Pt nanoparticles", *J. Catalysis* **2012**, 291, 69.
2. S. Guo, S. Dong, E. Wang, "Gold/Platinum hybrid nanoparticles supported on multiwalled carbon nanotube/silica coaxial nanocables: preparation and application as electrocatalysts for oxygen reduction", *J. Phys. Chem. C* **2008**, 112, 2389.
3. J. Zhang., K. Sasaki, E. Sutter, R.R. Adzic, "Stabilization of platinum oxygen reduction electrocatalysts using gold clusters", *Science* **2007**, 315, 220.
4. Z. Peng, H. Yang, "Synthesis and oxygen reduction electrocatalytic property of Pt-on-Pd bimetallic heteronanostructures", *J. Am. Chem. Soc.* **2009**, 131, 7542.
5. N. Tian, Z.-Y. Zhou, S.-G. Sun, Y. Ding, Z.L. Wang, "Synthesis of tetrahedral platinum nanocrystals with high-index facets and high electro-oxidation activity", *Science* **2007**, 316, 732.
6. B. Lim, X. Lu, M. Jiang, P.H.C. Camargo, E.C. Cho, E.P. Lee, Y. Xia, "Facile synthesis of highly faceted multi-octahedral Pt nanocrystals through controlled overgrowth", *Nano Lett.* **2008**, 8, 4043.
7. B. Lim, M. Jiang, J. Tao, P.H.C. Camargo, Y. Zhu, Y. Xia, "Shape controlled synthesis of Pd nanocrystals in aqueous solutions", *Adv. Funct. Mater.* **2009**, 19, 189.
8. E. Antolini, F. Cardellini, "Formation of carbon supported PtRu alloys: an XRD analysis", *J. Alloy Com.* **2001**, 315, 118.
9. T. Lopes, E. Antolini, E.R. Gonzalez, "Carbon supported Pt-Pd as an ethanol tolerant oxygen reduction electrocatalysts for direct ethanol fuel cells", *Int. J. Hydrogen Energ.* **2008**, 33, 5563.
10. E. Antolini, L. Giorgi, F. Cardellini, E. Passalacqua, "Physical and morphological characteristics and electrochemical behavior in fuel cells of PtRu/C catalysts", *J. Solid State Electrochem.* **2001**, 5, 131.
11. N. Markovic, H. Gasteiger, P.N. Ross, "Kinetics of oxygen reduction on Pt(hkl) electrodes: implications for the crystallite size effect with supported Pt electrocatalysts", *J. Electrochem. Soc.* **1997**, 144, 1591.
12. P. Urchaga, S. Baranton, C. Coutanceau, G. Jerkiewicz, "Electro-oxidation of CO on the Pt nanosurfaces: solution of the peak multiplicity puzzle", *Langmuir* **2012**, 28, 3658
13. S. Sun, G. Zhang, D. Geng, Y. Chen, R. Li, M. Cai, X. Sun, "A highly durable

platinum nanocatalyst for proton exchange membrane fuel cell: multiarmed starlike nanowire single crystal", *Angew. Chem. Int. Ed.* **2011**, 50,422.

14. R. O'Hayre, S.W. Cha, W. Colella, F.B. Prinz, "Fuel cell fundamentals", *John Wiley & Sons* **2006**.

15. W. Vielstich, A. Lamm, H.A. Gasteiger, "Handbook of fuel cells-fundamentals, Technology and applications", *Wiley & Sons* **2003**.

16. EG&G Technical Services, "Fuel cell handbook" 7th ed.; Parsons Inc., **2004**

17. J. Zhang, "PEM Fuel Cell Electrocatalysts and Catalyst Layers: Fundamentals and Applications", *Springer: London*, **2008**.

18. K.R. Cooper, V. Ramani, J. M. Fenton, H.R. Kunz, "Experimental Methods and Data Analyses for Polymer Electrolyte Fuel Cells", *Scribner Associates Inc.: North Carolina*, **2005**.

19. E.J. Antolini, *Mater. Sci.* **2003**, 38, 2995. (b)

20. Kloke, A.; Stetten, F. von; Zengerle, R.; Kerzenmacher, S. *Adv. Mater.* **2011**, 23, 4976.

21. Wang, C.; Daimon, H.; Onodera, T.; Koda, T.; Sun, S. *Angew. Chem., Int. Ed.* **2008**, 47, 3588.

22. Mazumder, V.; Lee, Y.; Sun, S. *Adv. Funct. Mater.* **2010**, 20, 1224.

23. Stamenkovic, V. R.; Fowler, B.; Mun, B. S.; Wang, G.; Ross, P. N.; Lucas, C. A.; Markovic, N. M. *Science* **2007**, 315, 493.

24. Lim, B.; Jiang, M.; Camargo, P. H.; Cho, E. C.; Tao, J.; Lu, X.; Zhu, Y.; Xia, Y. *Science* **2009**, 324, 1302.

25. Stamenkovic, V. R.; Mun, B. S.; Arenz, M.; Mayrhofer, K. J. J.; Lucas, C. A.; Wang, G.; Ross, P. N.; Markovic, N. M. *Nat. Mater.* **2007**, 6, 241.

26. Wang, C.; Chi, M.; Wang, G.; Vliet, D. van der; Li, D.; More, K.; Wang, H.-H.; Schlueter, J. A.; Markovic, N. M.; Stamenkovic, V. R. *Adv. Funct. Mater.* **2011**, 21, 147.

27. Wu, J.; Zhang, J.; Peng, Z.; Yang, S.; Wagner, F. T.; Yang, H. *J. Am. Chem. Soc.* **2010**, 132, 4984.

28. Zhang, J.; Yang, H.; Fang, J.; Zou, S. *Nano Lett.* **2010**, 10, 638. (g) Carpenter, M. K.; Moylan, T. E.; Kukreja, R. S.; Atwan, M. H.; Tessema, M. M. *J. Am. Chem. Soc.* **2012**, 134, 8535.

29. Wu, J.; Gross, A.; Yang, H. *Nano Lett.* **2011**, 11, 798. (i) Cui, C.; Gan, L.; Li, H.-H.; Yu, S.-H.; Heggen M.; Strasser, P. *Nano Lett.* **2012**, 12, 588.

30. Wang, D.; Xin, H. L.; Hovden, R.; Wang, H.; Yu, Y.; Muller, D. A.; DiSalvo, F. J.; Abruña, H. D. *Nat. Mater.* **2013**, 12, 81.

31. Wang, C.; Markovic, N. M.; Stamenkovic, V. R. *ACS Catal.* **2012**, 2, 891.

32. Bing, Y.; Liu, H.; Zhang, L.; Ghosh, D.; Zhang, J. *Chem. Soc. Rev.* **2010**, *39*, 2184.
33. Marković, N. M.; Schmidt, T. J.; Stamenković, V.; Ross, P. N. *Fuel Cells* **2001**, *1*, 105.
34. Chen, S.; Ferreira, P. J.; Sheng, W.; Yabuuchi, N.; Allard, L. F.; Shao-Horn, Y. *J. Am. Chem. Soc.* **2008**, *130*, 13818.
35. Kim, J.; Lee, Y.; Sun, S. *J. Am. Chem. Soc.* **2010**, *132*, 4996. (p) Wang, C.; Chi, M.; Li, D.; Strmcnik, D.; Vliet, D. van der; Wang, G.; Komanicky, V.; Chang, K. C.; Paulikas, A. P.; Tripkovic, D.; Pearson, J.; More, K. L.; Markovic, N. M.; Stamenkovic, V. R. *J. Am. Chem. Soc.* **2011**, *133*, 14396.
36. Guo, S.; Sun, S. *J. Am. Chem. Soc.* **2012**, *134*, 2492.
37. Jeon, T.-Y.; Yoo, S. J.; Cho, Y.-H.; Lee, K.-S.; Kang, S. H.; Sung, Y.-E. *J. Phys. Chem. C* **2009**, *113*, 19732.
38. Loukrakpam, R.; Luo, J.; He, T.; Chen, Y.; Xu, Z.; Njoki, P. N.; Wanjala, B. N.; Fang, B.; Mott, D.; Yin, J.; Klar, J.; Powell, B.; Zhong, C.-J. *J. Phys. Chem. C* **2011**, *115*, 1682.
39. Mun, B. S.; Watanabe, M.; Rossi, M.; Stamenkovic, V.; Markovic, N. M.; Ross, P. N. *Surf. Rev. Lett.* **2006**, *13*, 697.
40. Sasaki, K.; Naohara, H.; Choi, Y.; Cai, Y.; Chen, W.-F.; Liu, P.; Adzic, R. R. *Nat. Commun.* **2012**, *3*, 1115.
41. Nilekar, A. U.; Xu, Y.; Zhang, J.; Vukmirovic, M. B.; Sasaki, K.; Adzic, R. R.; Mavrikakis, M. *Top Catal.* **2007**, *46*, 276.
42. Park, J.; An, K.; Hwang, Y.; Park, J.-G.; Noh, H.-J.; Kim, J.-Y.; Park, J.-H.; Hwang, N.-M.; Hyeon, T. *Nat. Mater.* **2004**, *3*, 891.
43. An, K.; Lee, N.; Park, J.; Kim, S. C.; Hwang, Y.; Park, J.-G.; Kim, J.-Y.; Park, J.-H.; Han, M. J.; Yu, J.; Hyeon, T. *J. Am. Chem. Soc.* **2006**, *128*, 9753.
44. Park, J.; Joo, J.; Kwon, S. G.; Jang, Y.; Hyeon, T. *Angew. Chem., Int. Ed.* **2007**, *46*, 4630.
45. Wang, D. S.; Li, Y. D. *J. Am. Chem. Soc.* **2010**, *132*, 6280.
46. W.-P. Zhou, X. Yang, M.B. Vukmirovic, B.E. Koel, J. Jiao, G. Peng, M. Mavrikakis, R. Adzic, "Improving Electrocatalysts for O₂ reduction by fine tuning the Pt-support interaction: Pt monolayer on the surfaces of a Pd₃Fe(111) single-crystal alloy", *J. Am. Chem. Soc.* **2009**, *131*, 12755.
47. M.-H Shao, K. Sasaki, R.R. Adzic, "Pd-Fe nanoparticles as electrocatalysts for oxygen reduction", *J. Am. Chem. Soc.* **2006**, *128*, 3526.
48. D. Wang, H.L. Xin, H. Wang, Y. Yu, E. Rus, D.A. Muller, F.J. Disalvo, H.D. Abruna, "Facile synthesis of carbon-supported Pd-Co core-shell nanoparticles as oxygen

reduction electrocatalysts and their enhanced activity and stability with monolayer Pt decoration", *Chem. Mater.* **2012**, 24,2274.

49. Y. Suo, L. Zhuang, J. Lu, "First principle considerations in the design of Pd-alloy catalysts for oxygen reduction", *Angew. Chem. Int. Ed.* **2007**,46,2862.

50. M. Shao, P. Liu, J. Zhang, R. Adzic, "Origin of enhanced activity in palladium alloy electrocatalysts for oxygen reduction reaction", *J. Phys. Chem. B* **2007**, 111, 6772.

51. T. Ghosh, M.B. Vukmirovic, F.J. Disalvo, R.R. Adzic, "Intermetallics as novel supports for Pt monolayer O₂ reduction electrocatalysts: potential for significantly improving properties", *J. Am. Chem. Soc.* **2010**, 132, 906.

51. S.B. Ziemecki, G.A. Jones, D.G. Swartzfager, R.L. Harlow, "Formation of interstitial Pd-C phase by interaction of ethylene, acetylene, and carbon monoxide with palladium", *J. Am. Chem. Soc.* **1985**, 107, 4547.

52. J. Kudrnovsky, V. Drchal, S. Khmelevskiy, I. Turk, "Effects of atomic magnetic order on electronic transport in Pd-rich Pd-Fe alloys", *Phys. Review B* **2011**, B84, 214436.

53. Y. Pan, F. Zhang, K.Wu, Z. Lu, Y. Chen, Y. Zhou, Y. Tang, T. Lu, "Carbon supported palladium-iron nanoparticles with uniform alloy structure as methanol-tolerant electrocatalysts for oxygen reduction reaction", *Int. J. Hydrogen Energy* **2012**, 37, 2993.

54. M. Neergat, V. Gunasekar, R. Rahul, "Carbon-supported Pd-Fe electrocatalysts for oxygen reduction reaction", *J. Electro. Chem.* **2011**, 658, 25.

55. V. Stamenkovic, B.S. Mun, K.J.J. Mayhofer, P.N. Ross, N.M. Markovic, J. Rossmeisl, J. Greeley, J.K. Norskov, "Changing the activity of electrocatalysts for oxygen reduction by tuning the surface electronic structure", *Angew. Chem. Int. Ed.* **2006**, 45, 2897.

56. J. Zhang, M.B. Vukmirovic, Y. Xu, M. Mavrikakis, R.R. Adzic, "Controlling the catalytic activity of platinum monolayer electrocatalysts for oxygen reduction with different substrates", *Angew. Chem. Int. Ed.* **2005**, 44, 2132.

57. Y. Okamoto, O. Sugino, "Hyper-volcano surface for oxygen reduction reactions over noble metals", *J. Phys. Chem.* **2010**, 114, 4473.

58. T.H. Yu, Y. Sha, B.V. Merinov, W.A. Goddard, "improved non Pt alloys for the oxygen reduction reaction at fuel cell cathodes predicted from quantum mechanics", *J. Phys. Chem. C* **2010**, 114, 11527.

59. J.K. Norskov, J. Rossmeisl, A. Logadottir, L. Lindqvist, J.R. Kitchin, T. Bligaard, H. Jonsson, "Origin of the overpotential for oxygen reduction at the fuel-cell cathode", *J. Phys. Chem. B* **2004**, 108, 17886.

60. K. Kimijima, A. Hayashi, S. Umemura, J. Miyamoto, K. Sekizawa, T. Yoshida, I. Yagi, "Oxygen reduction reactivity of precisely controlled nanostructured model catalysts", *J. Phys. Chem. C* **2010**, 114, 14675.
61. Y.-C. Yeh, H.M. Chen, R.-S. Liu, K. Asakura, M.-Y. Lo, Y.-M. Peng, T.-S. Chan, J.-F. Lee, "Pd-C-Fe nanoparticles investigated by X-ray absorption spectroscopy as electrocatalysts for oxygen reduction", *Chem. Mater.* 2009, 21, 4030.
62. V. Mazumder, M. Chi, K.L. More, S. Sun, "Synthesis and characterization of multimetallic Pd/Au and Pd/Au/FePt core/shell nanoparticles", *Angew. Chem.. Int. Ed.* **2010**, 49, 9368.
63. T.-Y. Jeon, S.J. Yoo, H.-Y. Park, S.-K. Kim, S. Lim, D. Peck, D.-H. Jung, Y.-E. Sung, "Electrocatalytic effects of carbon dissolution in Pd nanoparticles", *Langmuir*, **2012**, 28, 3664.
64. S.J. Hwang, S.J. Yoo, J. Shin, Y.-H. Cho, J.H. Jang, E. Cho, Y.-E. Sung, S.W. Nam, T.-H. Lim, S.-C. Lee, S.-K. Kim, "Supported core@shell electrocatalysts for fuel cell: close encounter with reality" *Scientific Reports* **2013**, 3, 1309.

Chapter 4

Conclusions

Over the past two decades nanocatalysts have drawn immense amount of interest as the key to overcome the obstacle of commercialization of PEMFCs. Pt nanocatalyst was the most widely used nanocatalyst for PEMFC in anode and cathode. However, the cost of Pt itself was very high for the commercialization and ORR activity of Pt nanocatalyst required improvement. Therefore, the catalyst that can overcome the high cost, sluggish reaction of oxygen reduction reaction (ORR), and low durability is considered as a new catalyst for PEMFC.

In the beginning of the nanocatalysts study it was concentrated on forging high oxygen reduction activity by tuning the surface structure of the nanocatalysts, size and shape of the nanocatalysts, and alloying different metals. The enhanced ORR activity of Pt skin on single crystal substrates had been suggested applying various Pt skin electrocatalyst which was prepared using Cu displacement reaction. As a result, satisfactory catalytic activity was obtained; however, in contrast to evolution of catalytic activity insufficient improvement of the stability was found. Resolving the insufficient stability of the nanocatalysts may play a role as an engine to boost up the nanocatalysts study to a second stage. Therefore, many researchers did empirical and theoretical study to reconcile the high activity and high stability of the nanocatalysts. Recently, computational screening of

Pt coated on various core materials was scrutinized to select the suitable nanocatalysts for high activity and high stability, and enhanced stability of PtNi tuning the composition and surface morphology of PtNi.

In this thesis, the effect of structure enhancement on the nanocatalysts for ORR activity was investigated using carbon supported nanostructure catalysts which have different nanostructure and PdFe core decorated by Pt effect in the catalyst surfaces. The nanocatalyst with high activity and high stability were formed in four different ways: 1) synthesis of 20 nm Pt cluster formed with small 5 nm sized Pt nanoparticles, 2) urchin like structured PtNi with formed with 1-D rod 3) post thermal treatment of Pd-Fe alloy nanoparticles under air and H₂ gas which led to Pd rich surface Pd-Fe core compositions with high alloying degree 4) decorating Pd-Fe alloy nanoparticles with Pt applying hydroquinone method.

Pt cluster can be considered as a break through catalyst for the commercialization of PEMFC. Because it possess high activity for oxygen reduction and strong resistance against high potential. Therefore, we synthesized Pt cluster by using organic solvent and applied HDD as a reducing agent to control the reduction of the Pt(acac)₂ and long-chain amine HDA as a main capping agent. Pt cluster had a strong durability due to dominant (111) facet. The ORR polarization curves of Pt cluster and commercial Pt, the half wave potential ($E_{1/2}$) of Pt cluster is (0.92 V) located 0.03 V higher than that of the commercial Pt (0.89 V), construing that ordered single crystalline phase, small proportion of low-coordinated sites, and lattice contraction gained by the porous structure are the factors for

the ORR enhancement.

We synthesized different composition of urchin like Pt-Ni nanostructures by controlled one-pot NMIR process. The composition control of Pt-Ni nanostructures was achieved by varying molar ratio of Pt(acac)₂ and Ni(acac)₂. Cyclic voltammetry method was used to investigate the difference of electrochemical properties between urchin like Pt_xNi nanostructures and commercial Pt₃Ni. Intriguingly, the oxide formation/reduction potential of urchin like Pt₃Ni is more positive than that of commercial Pt₃Ni, which the adsorption may be attributed to a growth of 1D structure. Specific activity and mass activity of urchin like Pt₃Ni nanostructures was 2.4 times and 2.4 times of that of that of commercial Pt₃Ni. It is known that (111) plane exhibits better activity than (100) plane in Pt-Ni bimetallic compounds. The enhanced ORR activity of urchin like Pt₃Ni nanostructures is caused by the substantial amount of higher electrochemical active (111) plane on the surface in nanostructures. 1-D arms in urchin like structure are consisted of (111) planes rather than (100) planes. XRD profile also manifests the unique characteristic of urchin like Pt₃Ni nanostructures, which the increased sharpness of the (111) peak has a good correspondence with the increment of (111) facets.

A new catalyst to enhance the ORR activity and to reduce the manufacturing cost PdFe was proposed. We investigated that PdFe with post heat treatment can exceed the ORR activity of the Pt due to the metallic phase change of Pd and Fe. PdFe nanoparticles were synthesized via two-step reduction method. Pd-Fe alloy nanoparticles were synthesized by polyol reducing method using 1,2-propanediol as solvent and reducing agent and

oleylamine as a stabilizer. After the synthesis PdFe samples were post heat treated in air and H₂ atmosphere at 300 °C and 500 °C. XRD data manifested that the PdFe alloying degree increased as the post heat treatment temperature increases. Analysis of Pd K edge and Fe K edge XANES data showed that the oxidation state of Pd stays as a metallic phase before and after of the post heat treatment but the oxidation state of Fe shifts from Fe oxide phase to metallic phase after the post heat treatment. Therefore, for the bimetallic catalyst the amount of metallic phase of each atoms play an important role to enhance the alloying degree and ORR activity. As prepared Pd₁Fe₃, Pd₁Fe₁, and Pd₃Fe₁ samples half wave potential values were 0.71 V, 0.75 V and 0.78 V, respectively. In contrast, 500 °C post heat treated PdFe samples exhibited dramatic increase in ORR half wave potential. The half-wave potentials increased in following order: Pd₃Fe₁ < Pd₁Fe₃ < Pd₁Fe₁ (0.77 V < 0.89 V < 0.92 V). Through the electrochemical characterization of PdFe and post heat treated PdFe samples using cyclic voltammetry and ORR measurement we found a correlation between metallic phase and enhancement of ORR activity.

Core-shell is a well known structure to enhance the ORR activity of core material. In general, cheap metals are chosen as a core material and Pt is selected for shell material to improve the Pt utilization. The surface composition and particle size of PdFe core-Pt shell with different Pt loadings were measured by XRD and reductive adsorption of CO and CO₂. As the loading of Pt increases the particle size grows to 3.24 nm and CO and CO₂ oxidation peak of PdFe@Pt shifts toward to that of Pt.

These catalysts shed a new light on PEMFC, that tuning the structure of the catalyst with high proportion of (111) facet and metallic phase can lead to the high activity and durability.

국 문 초 록

지속 가능한 에너지원 중에 하나인 고분자 전해질 연료전지의 상용화를 위해 오래 전부터 나노촉매에 대한 연구가 활발히 진행되어 왔었다. 백금이 고분자 전해질 연료전지의 산화극과 환원극에 가장 널리 쓰이는 나노촉매인데 가격이 비싸고 고전압에서 안정성이 떨어지는 단점의 개선과 함께 산소 환원 반응의 향상이 요구된다. 따라서 고분자 전해질 연료전지의 환원극 촉매층에서 산소환원 반응이 원활하게 일어날 수 있도록 산소환원 반응 과정에서 촉매와 산소종간의 흡착 에너지가 낮은 특징을 가지며 높은 과전압에서도 오래 이용할 수 있는 안정성을 갖는 나노촉매의 개발이 필요하다. 그리고 위와 같은 장점을 가지는 촉매의 개발을 위해 표면 구조, 모양과 크기의 개선과 다른 금속간의 합금에 관한 연구가 활발히 이뤄지고 있다.

본 논문에서는 1) 클러스터 구조를 가지는 백금 나노촉매와 성게 모양을 가지는 백금-니켈 나노촉매를 통해 나노촉매의 구조 개선이 산소환원 반응활성과 고전압에서의 안정성에 미치는 영향 규명 2) 팔라듐-철 합금 나노촉매의 금속 산화 정도와 산소환원 반응간의 상관관계 규명 3) 팔라듐-철 위에 백금을 코팅 함으로서 발생하는 표면 구조 변화의 측정에

대해서 논하고자 한다.

최근에 백금 클러스터의 합성에 관한 연구가 있어왔고, 위와 같은 구조를 가지는 촉매를 산소환원 반응에 이용하면 활성이 뛰어난과 동시에 안정성에서도 큰 향상이 있다는 결과가 몇몇 연구자들에 의해 알려졌다. 하지만 수용액 상태에서 합성을 하였기 때문에 유기 용액 상태에서 합성을 할 때 보다 안정성과 산소환원 반응 면에서 부족할 것임을 예측할 수 있었다. 본 논문에서 백금 클러스터 구조는 유기 용액에서 아민계열의 캡핑제와 백금 전구체 간의 흡착력을 이용하여 합성되었다. 이렇게 합성된 백금 클러스터의 안정성은 ADT를 통해서 측정을 하였고 산소환원 반응 향상과 고전압에서의 안정성 증가 원인은 XANES와 분석을 통해서 규명을 하였다. 백금 클러스터와 상용 백금 촉매를 0.6 볼트에서 1.1 볼트 사이를 10,000 사이클 동안 구동한 다음 측정된 전기활성면적을 비교해 보면 백금 클러스터는 4.11 % 의 감소율을 보였고 상용 백금 촉매는 63.64 % 의 감소율을 보였다. 백금 클러스터가 이처럼 높은 안정성을 가질 수 있게 된 이유로는 낮은 비율의 low coordinated site와 많은 비율의 (111) 때문이다. 크기가 작은 입자일수록 표면에서 low coordinated site가 증가되는데 이는 산소종과의 흡착력 증가를 수반하기 때문에 결과적으로 산소환원 반응의 감소를 가져온다. 그러나 백금 클러스터는 high coordinated site가 많기

때문에 산소종과의 흡착력이 작아서 결과적으로 산소와 흡착할 면적이 많아지게 되어서 산소환원 반응의 증가를 가져온다. 그리고 이는 XANES 분석에서 백금 클러스터의 white line intensity가 상용 백금 촉매의 white line intensity 보다 낮음으로써 확인할 수 있었다.

성계 모양을 가지는 백금-니켈 나노촉매 또한 (111) 면을 가지고 있는 1-D 가지들이 많기 때문에 상용 백금-니켈 대비 산소환원 반응과 안정성에서 향상된 결과를 보였다. 성계 모양 백금-니켈 나노촉매는 상용 백금-니켈 나노촉매 대비 2배 이상의 산소환원 반응 증가를 보였다. 그리고 0.6 볼트에서 1.1 볼트 사이를 4,000 사이클 동안 구동한 다음 측정된 전기활성면적을 비교해 보면 성계 모양 백금-니켈은 41.88 % 의 감소율을 보였고 상용 백금-니켈 촉매는 55.78 % 의 감소율을 보였다.

고분자 전해질 연료전지의 상용화 면에서 가격은 중요한 부분을 차지하며, 그 중에서 백금의 높은 가격은 큰 문제가 되고 있다. 본 논문에서는 팔라듐-철을 적절한 조합으로 합금시킨 후 열처리를 통해서 백금을 사용하지 않았음에도 상용 백금 촉매보다 높은 산소환원 반응 활성을 가지는 결과를 얻었다. 다양한 조성의 팔라듐-철 나노촉매 합성을 위해 유기 용액과 수소화붕소나트륨을 환원제로 사용하였다. XRD와 XANES 분석을 통해서 후 열처리로 인한 팔라듐-철 나노촉매의 금속 상태 변화를

확인할 수 있었다. 처음 합성 상태인 팔라듐-철 나노촉매 에서는 팔라듐과 철의 합금으로 인한 XRD 피크 이동을 확인할 수 없었다. 그러나 300 °C 와 500 °C 에서 열처리 한 후의 팔라듐-철 나노촉매의 XRD 데이터 에서는 팔라듐과 철의 합금으로 인해 높은 각도로 이동하는 결과를 얻을 수 있었다. 이 현상을 좀더 자세히 규명하기 위해 XANES 분석을 이용하여 팔라듐과 철의 K edge 변화를 관찰하였다. 팔라듐 K edge는 처음 합성 상태와 열처리 후의 상태에서도 큰 차이를 보이지 않은 반면에 철 K edge는 처음 합성 상태에서는 부분적으로 산화철이 많은 나노촉매였는데 후 열처리를 한 후에는 산화철이 철로 대부분 환원됨을 확인할 수 있었다. 그리고 철의 금속량 증가와 XRD 피크의 높은 각 이동은 서로간의 상관관계가 있음을 입증하였다.

코어-셸 구조는 값싼 물질을 코어로 쓰고 백금을 셸로 이용함으로써 산소환원 반응의 증가와 더불어 백금의 이용률을 높이는 효과를 가지는 구조이다. XRD 분석을 통하여 팔라듐-철-코어 백금-셸의 크기 변화를 측정하였고 일산화탄소와 이산화탄소의 산화 반응을 이용하여 백금의 양이 증가할수록 전기화학적으로 어떠한 변화가 일어나는지 알아보았다. 팔라듐-철-코어 위에 백금의 코팅 양이 증가할수록 입자 크기는 2.71 나노미터에서 3.24 나노미터로 증가하였다. 그리고 일산화탄소와

이산화탄소의 산화 반응에서도 백금의 코팅 양이 증가할수록 팔라듐-철의 성질을 나타내는 높은 전압에서의 산화 피크가 백금의 특성을 보여주는 낮은 전압으로의 산화 피크로 이동하는 현상을 관찰 할 수 있었다.

주요어: 연료전지, 산소환원 반응, 백금, 클러스터, 팔라듐-철, 코어-셸

학번: 2009-31266

감사의 글

2007 년부터 시작되었던 대학원생이라는 항해가 6 년이라는 긴 시간 끝에 마지막을 향해 달려가고 있습니다. 지난 6 년 동안 PEEL 이라는 랩실에서 겪었던 희로애락들이 주마등처럼 스쳐 지나갑니다. 랩실 생활을 통해서 제 인생 처음으로 뮤지컬을 봤었고 처음으로 축구화를 샀었고 처음으로 20 명이 넘는 사람들과 하루의 시작과 끝을 함께 했던 거 같습니다.

하지만 많은 부분에서 부족한 저였기에 대학원 생활을 무사히 마치고 결별이 이룩하는 축복 속에서 졸업을 할 수 있을까 걱정하며 잠 못 이룰 때가 많았습니다. 하지만 우리의 인생에서 길다면 길다고 할 수 있고 짧다면 짧다고 할 수 있는 6 년이라는 시간 동안 제가 무사히 항해를 마칠 수 있게 된 것은 모진 풍파에도 흔들리지 않고 쓰러지지 않도록 항상 저에게 정신적으로나 물질적으로 도움을 주신 여러분이 계시기에 가능했었습니다.

먼저 저의 대학원 생활 처음부터 끝까지 한결같이 때로는 아버지와 같은 인자함으로 때로는 선배 연구자로서 냉철하게 저의 연구를 지도편달 해주신 존경하는 성영은 교수님께 고개 숙여 감사 드립니다. 그리고 바쁘신 와중에도 저의 박사 학위 논문 지도와 심사를 해주신 이종협 교수님, 김도희 교수님, 탁용석 교수님과 유성중 박사님께 진심으로 감사 드립니다.

아마 마지막이 될지도 모르기 때문에 실험실 멤버들 (영훈, 민제, 승호, 정우, 인영, 윤식, 옥희 누나, 민건, 지현, 경재, 정진이형, 동영, 인환, 정준, 민경, 귀룡, 명재, 대혁, 민정, 민형, 진수, 애화, 지은, 재혁, 영민이형, 해나, 진이, last but not least 영원) 전체에게도 남은 학위기간 잘 마치길 바라는 마음과 함께 감사의 마음을 전합니다. 그리고 지금은 졸업하고 각자의 길에서 최선을 다하고 계시는 저의 멘토이신 선배님들 (인수형, 국승이형, 윤채형, 주완이형, 윤환이형)과 동갑내기로서 언제나 편안함을 선사해준 친구들 (남기, 희영, 재엽, 선하)에게도 감사의 뜻을 전합니다. 그리고 서울대학교라는 생경한 곳에서 저의 얼굴에 웃음꽃이 저물지 않도록 옆에서 든든한 동반자가 되어준 다른 랩실 동생들 (태환, 형태, 성진, 선호)에게도 고맙다는 말을 하고 싶습니다.

마지막으로 저를 나아주시고 길러주시고 호기심을 가지고 세상을 바라보는 눈과 꿈에 책임을 지는 용기를 갖게끔 해주신 저의 부모님께 감사 드립니다.

박사로서의 첫 걸음을 내딛게 되는 저에게 세상 그 어느 누구보다 많은 축하를 건네준 나의 사랑스런 이란성 쌍둥이 동생 소영이와 광욱이 그리고 매제에게도 감사의 말을 전합니다.

끝은 또 하나의 시작이라는 말처럼 저의 대학원 생활은 여기서 끝나지만 대학원 생활 동안 보고 듣고 느낀 경험들이 제가 앞으로의 인생에서 새로운 시작을 할 때 두려움 없이 인생을 최고로 여행할 수 있는 밑거름이 될 거라 믿습니다.

이 글을 쓰고 있는 지금 제가 좋아하는 미당 서정주 시인의 ‘연꽃 만나고 가는 바람 같이’의 한 구절이 생각이 납니다.

연꽃
만나러 가는
바람 아니라
만나고 가는 바람 같이.....

PEEL 여러분이라는 연꽃을 만날 수 있어서 저는 행복했습니다.

2013 년 8 월 1 일

최 광 현 올림